Herschel[★] and JCMT observations of the early-type dwarf galaxy NGC 205

I. De Looze,[1]† M. Baes,[1] T. J. Parkin,[2] C. D. Wilson,[2] G. J. Bendo,[3] M. Boquien,[4]
A. Boselli,[4] A. Cooray,[5] D. Cormier,[6] J. Fritz,[1] F. Galliano,[6] W. Gear,[7] G. Gentile,[1]
V. Lebouteiller,[6] S. C. Madden,[6] H. Roussel,[8] M. Sauvage,[6] M. W. L. Smith,[7]
L. Spinoglio,[9] J. Verstappen[1] and L. Young[10]

[1]*Sterrenkundig Observatorium, Universiteit Gent, Krijgslaan 281 S9, B-9000 Gent, Belgium*
[2]*Department of Physics & Astronomy, McMaster University, Hamilton, ON L8S 4M1, Canada*
[3]*UK ALMA Regional Centre Node, Jodrell Bank Centre for Astrophysics, School of Physics and Astronomy, University of Manchester, Oxford Road, Manchester M13 9PL*
[4]*Laboratoire d'Astrophysique de Marseille – LAM, Université d'Aix-Marseille & CNRS, UMR7326, 38 rue F. Joliot-Curie, 13388 Marseille Cedex 13, France*
[5]*Department of Physics & Astronomy, University of California, Irvine, CA 92697, USA*
[6]*Laboratoire AIM, CEA/DSM- CNRS – Université Paris Diderot, Irfu/Service d'Astrophysique, 91191 Gif sur Yvette, France*
[7]*School of Physics and Astronomy, Cardiff University, Queens Buildings, The Parade, Cardiff CF24 3A A*
[8]*Institut d'Astrophysique de Paris, UMR 7095 CNRS, Université Pierre et Marie Curie, 98 bis Boulevard Arago, F-75014 Paris, France*
[9]*Istituto di Fisica dello Spazio Interplanetario, INAF, Via del Fosso del Cavaliere 100, I-00133 Roma, Italy*
[10]*Physics Department, New Mexico Institute of Mining and Technology, Socorro, NM 87801, USA*

ABSTRACT

We present *Herschel* dust continuum, James Clerk Maxwell Telescope CO (3–2) observations and a search for [C II] 158 μm and [O I] 63 μm spectral line emission for the brightest early-type dwarf satellite of Andromeda, NGC 205. While direct gas measurements [$M_g \sim 1.5 \times 10^6$ M$_\odot$, H I + CO (1–0)] have proven to be inconsistent with theoretical predictions of the current gas reservoir in NGC 205 ($>10^7$ M$_\odot$), we revise the missing interstellar medium mass problem based on new gas mass estimates (CO (3–2), [C II], [O I]) and indirect measurements of the interstellar medium content through dust continuum emission.

Based on *Herschel* observations, covering a wide wavelength range from 70 to 500 μm, we are able to probe the entire dust content in NGC 205 ($M_d \sim 1.1$–1.8×10^4 M$_\odot$ at $T_d \sim$ 18–22 K) and rule out the presence of a massive cold dust component ($M_d \sim 5 \times 10^5$ M$_\odot$, $T_d \sim 12$ K), which was suggested based on millimetre observations from the inner 18.4 arcsec. Assuming a reasonable gas-to-dust ratio of $\sim$400, the dust mass in NGC 205 translates into a gas mass $M_g \sim 4$–7×10^6 M$_\odot$. The non-detection of [O I] and the low $L_{[C II]}$-to-$L_{CO(1-0)}$ line intensity ratio ($\sim$1850) imply that the molecular gas phase is well traced by CO molecules in NGC 205. We estimate an atomic gas mass of 1.5×10^4 M$_\odot$ associated with the [C II] emitting photodissociation regions in NGC 205. From the partial CO (3–2) map of the northern region in NGC 205, we derive a molecular gas mass of $M_{H_2} \sim 1.3 \times 10^5$ M$_\odot$. Upon comparison with the molecular gas mass estimated from CO (1–0) observations ($M_{H_2} \sim 6.9 \times 10^5$ M$_\odot$), we find most of the H_2 gas in NGC 205 to be locked in diffuse regions of low density and/or temperature, characteristic for an interstellar medium with little star formation activity.

New total gas mass estimates from *Herschel* dust continuum (4–7×10^6 M$_\odot$), *Herschel* [C II] line spectroscopic mapping (1.5×10^4 M$_\odot$) and James Clerk Maxwell Telescope CO (3–2) observations (7×10^5 M$_\odot$), including the H I mass ($M_{H I} \sim 4.0 \times 10^5$ M$_\odot$) and a correction

---

for heavier elements, confirm the deficiency of the interstellar medium (gas+dust) in the inner regions of NGC 205, which is predicted to contain at least $>10^7$ M$_\odot$ of gas if we assume a reasonable star formation efficiency of 10 per cent and account for the mass return from planetary nebulae. In an attempt to explain the missing interstellar medium mass problem, we claim that efficient supernova feedback capable of expelling gas from the inner, star-forming regions to the outer regions and/or tidal interactions with M31 stripping the gas component from the galaxy provide the best explanation for the removal of a significant amount of gas and dust from NGC 205.

Key words: ISM: evolution – galaxies: dwarf – galaxies: formation – galaxies: individual: NGC 205 – Local Group – infrared: ISM.

1 INTRODUCTION

85 per cent of all galaxies are located outside galaxy clusters, among which half reside in groups (Karachentsev 2005). Therefore, studying group environments is of great importance to learn more about the habitats for an important fraction of galaxies. The Local Group is of particular interest for studies of low surface brightness galaxies, since galaxies at the low-luminosity end often remain undetected in more distant group structures. Moreover, the Local Group allows probing the interstellar medium (ISM) of its residents at high resolution and, at the same time, offers a wealth of ancillary data, it being one of the best studied areas on the sky. Studying the properties of the ISM and metal enrichment in metal-poor dwarf galaxies offers a promising way to learn more about the conditions in the early Universe and the evolution of dwarf galaxies throughout the history of the universe.

Among the low surface brightness galaxies in the Local Group, the dwarf satellite NGC 205 ($\sim$824 kpc; McConnachie et al. 2005) of the Andromeda galaxy is of particular importance due to its relatively low metal abundance ($Z \sim 0.13$ Z$_\odot$; Richer & McCall 2008), interesting star formation history and indications of a tidal encounter with its massive companion M31. Although photometrically classified as a dwarf elliptical galaxy (de Vaucouleurs et al. 1991), the formation processes for NGC 205 seem more closely related to the dwarf spheroidal galaxy population (transformed from late-type galaxies through internal and environmental processes) rather than to merger remnants, thought to be the main driver for the formation of genuine ellipticals (Kormendy et al. 2009). The star formation history in NGC 205 has been studied extensively (Baade 1951; Hodge 1973; Bertola et al. 1995; Davidge 2003). An old stellar population (10 Gyr; Bica, Alloin & Schmidt 1990) dominates the overall stellar content of the dwarf galaxy, and a plume of bright blue star clusters in the central region of NGC 205 was already identified $\sim$60 years ago (Baade 1951; Hodge 1973).

1.1 Theoretical gas mass predictions

Combining observations of this young stellar population with adequate model assumptions has provided several independent theoretical predictions of the current gas content in NGC 205. Such predictions need to account for both the leftover gas reservoir after an epoch of star formation activity and the build-up of gas returned to the ISM by the evolved stellar population since the last starburst episode.

The leftover gas reservoir is probed through observations of the young stellar population providing an estimate of the total gas mass consumed during the last epoch of star formation. Usually, it is assumed that a star formation efficiency (SFE) of 10 per cent is

reasonable (e.g. Boylan-Kolchin, Bullock & Kaplinghat 2012; Martín-Manjón et al. 2012). From observations of both the nucleus and a region about 1 arcmin north of the nucleus with the *International Ultraviolet Explorer* (*IUE*) within an aperture of 10×20 arcsec^2, Wilcots et al. (1990) report a mass of young ($\sim$10 Myr old) stars $M_\star \sim 7 \times 10^5$ M$_\odot$ in NGC 205, which increases to $M_\star \sim 1.4 \times 10^6$ M$_\odot$ when extrapolating to the whole galaxy based on the stellar light contribution from OB stars (Wilcots et al. 1990) and also taking stellar masses <1 M$_\odot$ into account (Marleau et al. 2006). According to Bertola et al. (1995), NGC 205 was the host of a starburst starting $\sim$500 Myr ago involving a total stellar burst mass of $M_\star \sim 5.3 \times 10^7$ M$_\odot$, which is considerably higher than the estimate in Wilcots et al. (1990). More recently, Monaco et al. (2009) estimate $M_\star \sim 1.9 \times 10^5$ M$_\odot$ of stars to be produced between $\sim$62 and $\sim$335 Myr ago from observations of the nuclear 29×26 arcsec^2 region of NGC 205 with the Advanced Camera for Survey on-board the *Hubble Space Telescope* (*HST*), when assuming a Λ cold dark matter cosmological model. Although the estimated burst mass in Monaco et al. (2009) also includes lower mass stars ($M_\star < 1$ M$_\odot$), their value should be considered a lower limit of the total burst mass, since only a limited period (from 62 to 335 Myr ago) in the star formation history of NGC 205 is analysed and the observed area only corresponds to part of the region where the most recent star formation epoch took place.

The total amount of gas returned to the ISM by planetary nebulae is predicted to be $\sim$1.8 $\times 10^6$ M$_\odot$ (Welch, Sage & Mitchell 1998), following the prescriptions in Faber & Gallagher (1976) and assuming a time lapse of $\sim$500 Myr since the trigger of the last star formation activity. With the lower limit for the stellar burst estimates relying on 10 Myr old stars (Wilcots et al. 1990), the corresponding mass returned to the ISM since the formation of those young stellar objects can be predicted in a similar way ($\sim$3.6 $\times 10^4$ M$_\odot$). We only account for the mass loss from planetary nebulae since the mass lost from more massive stars is considered negligible due to their lower mass loss rate and shorter lifetime. Considering that the estimated burst mass critically depends on the model assumptions and is often biased by the sensitivity and coverage of the observations, we calculate a total burst mass during the last episode of star formation in the range $1.4 \times 10^6 \leq M_\star \leq 5.3 \times 10^7$ M$_\odot$, where the lower and upper limits correspond to stellar burst mass predictions from Wilcots et al. (1990) and Bertola et al. (1995), respectively. A burst mass of 1.4×10^6 M$_\odot$ would predict that the initial gas reservoir before the star formation episode was $M_g \sim 1.4 \times 10^7$ M$_\odot$ for an SFE of $\sim$10 per cent. Subtracting the 10 per cent of gas consumed into stars results in the leftover gas reservoir $M_g \sim 1.3 \times 10^7$ M$_\odot$ after the star formation epoch. When combining the leftover gas reservoir (i.e. the majority of the ISM mass) and mass loss by planetary

nebulae (depending on the assumed time lapse), we estimate a current gas content for NGC 205 ranging between 1.3×10^7 and $4.8 \times 10^8 \, M_\odot$.

1.2 Observations of the ISM content

Up to now, the total gas mass in NGC 205 was estimated from H I, CO (1–0) and dust continuum observations. A total H I mass of $4.0 \times 10^5 \, M_\odot$, scaled to a distance $D = 824 \, \text{kpc}$ for NGC 205, is reported in Young & Lo (1997) based on Very Large Array (VLA) observations covering the whole galaxy. Welch et al. (1998) detect CO (1–0) and CO (2–1) emission above the 3σ level from three and four positions, respectively, across the plane of NGC 205. Although a partial beam overlap occurs for the CO (1–0) observations (see red circles in Fig. 3), the covered area in the CO (1–0) observations is seven times larger than for the second CO (2–1) transition and, thus, provides a better estimate of the molecular gas content in NGC 205. While Welch et al. (1998) assumed a close to solar metallicity [implying a CO-to-H_2 conversion factor $X_{CO} = 2.3 \times 10^{20} \, \text{cm}^{-2} \, (\text{K km s}^{-1})^{-1}$; Strong et al. 1988], we apply a conversion factor of $6.6 \times 10^{20} \, \text{cm}^{-2} \, (\text{K km s}^{-1})^{-1}$, determined from the expression reported in Boselli, Lequeux & Gavazzi (2002) relating the X_{CO} factor to the oxygen abundance in a galaxy. This value for the X_{CO} factor is based on a metal abundance of $Z \sim 0.3 \, Z_\odot$ in the inner regions of NGC 205. Whereas the earlier reported metallicity value ($Z \sim 0.13 \, Z_\odot$) was obtained from averaging the oxygen abundances for 13 planetary nebulae in NGC 205 (Richer & McCall 2008) and thus refers to the whole galaxy, Sharina, Afanasiev & Puzia (2006) determined a mean metallicity [Z/H] $\sim -0.5 \pm 0.2$ for the central regions in NGC 205 from Lick indices. Considering that the last episode of star formation mainly occurred in the innermost regions, this gradient in metallicity and/or age is not surprising. A similar central increase in colour and metallicity has been noted in several early-type dwarf galaxies in the Fornax cluster (Koleva et al. 2009), and a population of dwarf elliptical galaxies (dEs) with central blue cores has been observed in the Virgo cluster (Lisker et al. 2006).

Additional CO (1–0) line emission was detected from a small area (beam size ~ 21 arcsec) observed in the south of NGC 205 (Young & Lo 1996; see green circle in Fig. 3). Combining those CO (1–0) observations, we obtain an estimate of $M_{H_2} = 6.9 \times 10^5 \, M_\odot$. This value for the molecular gas mass is, however, only a lower limit of the total H_2 mass, since the southern part of the galaxy is poorly covered by current CO (1–0) observations. Combining both H I and CO (1–0) observations, which were scaled by a factor of 1.4 to include helium, we derive a total gas mass $M_g \sim 1.5 \times 10^6 \, M_\odot$ for NGC 205, which is about one order of magnitude lower than the more modest theoretical predictions for the gas content. This deficiency in the gas content of NGC 205 is often referred to as the problem of the 'missing ISM mass' (Welch et al. 1998).

Although gas observations directly probe the ISM component of interest, the dependence of the X_{CO} conversion factor on the metallicity (Wilson 1995; Bolatto et al. 2008) and density of the gas (Shetty et al. 2011) and the optical thickness of the CO (1–0) line introduce an uncertainty on the estimate of the total gas mass. In particular, for metal-poor galaxies the molecular gas phase could be poorly traced by CO (Wilson 1995; Madden et al. 1997; Leroy et al. 2005, 2007). An alternative and promising method to measure the ISM mass in galaxies is to use observations of the continuum emission from dust (Hildebrand 1983; Guelin et al. 1993, 1995; Boselli et al. 2002; James et al. 2002; Eales et al. 2010; Eales et al. 2012).

Dust emission from NGC 205 was first detected with *IRAS* (Rice et al. 1988). NGC 205 was also the first early-type dwarf galaxy detected at millimetre (mm) wavelengths (Fich & Hodge 1991). Based on these *IRAS* data and 1.1 mm observations for the central 18 arcsec (21 ± 5 mJy) in NGC 205, Fich & Hodge (1991) estimated a dust mass of $M_d \sim 3 \times 10^3 \, M_\odot$ at a temperature of ~ 19 K. Using *ISO* observations, Haas (1998) obtained a total dust mass estimate of $4.9 \times 10^3 \, M_\odot$ at a temperature of ~ 20 K. Recently, Marleau et al. (2006) probed the dust emission from NGC 205 with *Spitzer* and found a dust mass in the range $M_d = 3.2$–$6.1 \times 10^4 \, M_\odot$ at a temperature of ~ 18 K. Taking the 1.1 mm observation of the core region into account, Marleau et al. (2006) found a dust component in the central regions at a temperature of $T_d \sim 11.6$, 16 times more massive, suggesting that a substantial amount of cold dust might be overlooked if one only takes *IRAS*, *ISO* and *Spitzer* observations into consideration. Unfortunately, only the central region was observed at 1.1 mm, and it could not be investigated whether such a putative cold dust component is present over the entire galaxy. Under the assumption that the colder dust is not only distributed in the central region, but is abundantly present in the entire galaxy, they estimated a total gas mass of $5 \times 10^7 \, M_\odot$ for a gas-to-dust ratio of 100. To probe this cold dust component, we need observations at wavelengths longwards of 160 μm (e.g. Gordon et al. 2010; Galametz et al. 2011). Longer wavelength data also allow us to constrain the Rayleigh–Jeans side of the dust spectral energy distribution (SED), from which a more robust temperature estimate for our SED model can be obtained. Probing this cold dust component is now possible with the *Herschel Space Telescope* (Pilbratt et al. 2010), covering a wavelength range from 70 up to 500 μm. Recent *Herschel* observations of nearby galaxies have demonstrated the presence of significant amounts of cold dust (e.g. Bendo et al. 2010, 2012a; Smith et al. 2010; Boquien et al. 2011b; Fritz et al. 2012).

In this paper, we present *Herschel* observations for NGC 205 taken in the frame of the Very Nearby Galaxy Survey (VNGS) and the *Herschel* Exploitation of Local Galaxy Andromeda (HELGA) projects, with the aim of making an inventory of all the dust in NGC 205. Furthermore, we report new gas mass measurements from James Clerk Maxwell Telescope (JCMT) CO (3–2) observations and *Herschel* [C II] 158 μm and [O I] 63 μm line spectroscopic mapping. From those new dust and gas mass estimates, we are able to revise the 'missing ISM' problem in NGC 205. In Section 2, the data and observing strategy from *Herschel* and JCMT observations are discussed. The corresponding data reduction procedures are outlined and a brief overview of the ancillary data set is given. Section 3 discusses the spatial distribution of gas and dust in NGC 205 (Section 3.1), the global flux measurements (Section 3.2) and the basic principles and results of the SED fitting procedure (Section 3.3). The JCMT CO (3–2) and PACS spectroscopy data are analysed in Section 3.4 and new estimates for the gas mass are determined. Section 4 reanalyses the missing ISM mass problem in NGC 205 (Section 4.1), discusses the implications of our results for the star formation conditions and properties of the ISM in the galaxy (Section 4.2) and makes a comparison with the other early-type dwarf companions of Andromeda (Section 4.3). Finally, Section 5 summarizes our conclusions.

2 OBSERVATIONS AND DATA REDUCTION

2.1 PACS photometry

We use data for NGC 205 taken as part of two *Herschel* Guaranteed Time Projects: the VNGS (PI: C. Wilson) and HELGA (PI: J. Fritz).

From the VNGS, we obtained PACS photometry (Poglitsch et al. 2010) at 70 and 160 μm (ObsID 1342188692, 1342188693) and SPIRE photometry (Griffin et al. 2010) at 250, 350 and 500 μm. PACS data were observed on 2009 December 29 and cover an area of 1° × 1° centred on NGC 205. This area was observed in nominal and orthogonal scan direction with four repetitions at a medium scan speed (20 arcsec s^{-1}).

The main scientific objective of HELGA (Fritz et al. 2012) focuses on dust in the extreme outskirts of the Andromeda Galaxy. Thanks to its large survey area, NGC 205 was covered in the field of two overlapping scan observations. HELGA observations were performed in the parallel fast scan mapping mode (60 arcsec s^{-1}), obtaining PACS 100, 160 μm and SPIRE 250, 350 and 500 μm photometry (ObsID 1342211294, 1342211309, 1342211319, 1342213207).

To reduce the PACS data, we used version 13 of the SCANAMOR-PHOS[1] (Roussel et al. 2012) map making technique. Before applying SCANAMORPHOS to the level 1 data, the raw data were pre-processed in *Herschel* Interactive Processing Environment (HIPE; Ott 2010) version HIPE 6.0.1196. Due to the different observing set-ups, the depth of the PACS observations is inhomogeneous among the different wavebands. For PACS observations at 70 and 100 μm, we only have data available from one survey (either VNGS or HELGA, respectively). This data set was finally reduced to obtain maps with a pixel size of 2 arcsec. The full width at half-maximum (FWHM) values of the PACS beams are ~6 arcsec and ~7 × 13 arcsec^2 at 70 and 100 μm, respectively. Due to the lower level of redundancy and the fast scan speed, the PACS 100 μm waveband was observed in the least favourable conditions, resulting in the largest uncertainty values and interference patterns affecting the observations (see Fig. 2, second panel on the top row). In the red filter (PACS 160 μm), NGC 205 was covered by both VNGS and HELGA in medium and fast scan speed, resulting in a FWHM for the PACS beam of ~12 arcsec and ~12 × 16 arcsec^2, respectively. Our final photometry map combines data from both *Herschel* projects at this overlapping wavelength with the aim of increasing the signal-to-noise ratio. The unmatched scan speeds prevent reducing both observations simultaneously, since the drift correction is calculated over a certain stability length which depends on the scan speed of the observation. Therefore, both data sets were reduced individually in SCANAMORPHOS, using the same astrometry for the final maps. Before combining both maps, we convolved them to the same resolution of the point spread function (PSF), to avoid issues with the different beam sizes in both observations. Finally, the separately reduced and convolved VNGS and HELGA maps at 160 μm were combined into one single map in IRAF, with the `imcombine` task. The images were produced with the latest version of the PACS calibration files (version 26) and divided by the appropriate colour correction factors (1.016, 1.034 and 1.075 at 70, 100 and 160 μm; see Müller, Okumura & Klaas 2011, for a power-law spectrum with β = 2). The background was also subtracted from the final PACS images. An estimate for the background was obtained from averaging the background flux within 100 random apertures (diameter = 4×FWHM). Random apertures were selected within an annulus centred on NGC 205 with inner radius of 5 arcmin and outer radius of 20 arcmin, avoiding regions with bright emission from background sources and M31. Once the random background apertures were selected, those same positions for aperture photometry were applied at all wavelengths.

[1] http://www2.iap.fr/users/roussel/herschel

2.2 SPIRE photometry

SPIRE data were observed on 2009 December 27 (ObsID 1342188661), obtaining two repetitions of nominal and orthogonal scans at medium scan speed (30 arcsec s^{-1}). For all SPIRE bands, data sets from both VNGS and HELGA projects were available and combined into one frame. In the same way as for SCANAMORPHOS, the continuous temperature variations are different for VNGS and HELGA observations. Therefore, the corresponding data are reduced separately before combining them into one map. The SPIRE data were largely reduced according to the standard pipeline (POF5_pipeline.py, dated 2010 June 8), provided by the SPIRE Instrument Control Centre (ICC). Divergent from the standard pipeline were the use of the *sigmaKappaDeglitcher* (instead of the ICC-default *waveletDeglitcher*) and the BriGAdE method (Smith et al., in preparation) to remove the temperature drift and bring all bolometers to the same level (instead of the default *temperatureDriftCorrection* and the residual, median baseline subtraction). Reduced SPIRE maps have pixel sizes of 6, 8 and 12 arcsec at 250, 350 and 500 μm, respectively. The FWHM of the SPIRE beams are 18.2, 24.5 and 36.0 arcsec at 250, 350 and 500 μm, respectively. SPIRE images are converted from MJy beam^{-1} to Jy pixel^{-1} units assuming beam areas of 423, 751 and 1587 arcsec^2 at 250, 350 and 500 μm, respectively. Since the calibration in the standard pipeline is optimized for point sources, we apply correction factors (0.9828, 0.9834 and 0.9710 at 250, 350 and 500 μm) to convert the K4 colour correction factors from point source to extended source calibration (SPIRE Observers' Manual 2011). Additionally, multiplicative colour correction factors (0.9924, 0.9991 and 1.0249 at 250, 350 and 500 μm) were applied and a correction factor of 1.0067 was used to update the fluxes in the 350 μm image to the latest v7 calibration product (SPIRE Observers' Manual 2011). SPIRE images were also background subtracted, in a similar way as for the PACS images.

2.3 PACS spectroscopy

PACS spectroscopy maps, [C II] 157.74 μm and [O I] 63 μm, were observed on 2011 February 14 (ObsID 1342214374, 1342214375, 1342214376). The [C II] observations cover the northern and the central area of NGC 205 (see Fig. 1), while two smaller [O I] maps are centred on the CO peak in the north and on the centre of NGC 205 (see Fig. 1).
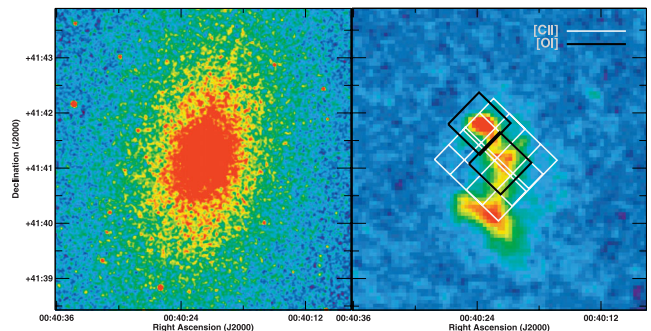

Figure 1. Left-hand panel: *K*-band image of NGC 205. Right-hand panel: PACS 160 μm image overlaid with the AORs for the [O I] (black, solid lineboxes) and [C II] (raster with white, solid lines) PACS line spectroscopy observations. The [O I] line was observed in the north of NGC 205, where the CO (1–0) emission peaks in the north, and in the central region of NGC 205. The [C II] observations cover both areas.

The PACS (Poglitsch et al. 2010) spectroscopic observations of NGC 205 were done in the chop/nod mode, and cover an area of 95 × 95 arcsec (3 × 3 pointings) and 47 × 47 arcsec (one pointing) for the [C II] (157.74 μm) and both [O I] (63 μm) maps, respectively. We used the largest chop throw of 6 arcmin to ensure we were not chopping on to extended source emission. The maps were processed from Level 0 to Level 2 using the standard pipeline in HIPE (version 7.0.0), with version (FM, 32) of the calibration files. Once the data are processed to Level 2, we used the PACSman program[2] (Lebouteiller et al. 2012) to perform line fits to the unbinned spectral data in each spatial pixel using a least-squares fitting routine, and to create integrated flux density maps of the results. For [C II], the flux map mosaic was created by projecting the individual rasters on to an oversampled grid. More details can be found in Lebouteiller et al. (2012).

2.4 Noise calculations

To determine the uncertainty on the PACS and SPIRE photometry data, we need to take into account three independent noise measurements. Aside from the most important uncertainty factor due to the calibration, the random background noise and the map making uncertainty contribute to the flux uncertainty as well. For the calibration uncertainty, values of 3, 3 and 5 per cent were considered for the PACS 70, 100 and 160 μm data, respectively (PACS Observer's Manual 2011). All SPIRE wavebands were assumed to have a calibration uncertainty of 7 per cent (Swinyard et al. 2010; SPIRE Observer's Manual 2011). An estimate for the background noise is derived by taking 100 random apertures in the field around the galaxy (i.e. the same apertures used to determine the background), calculating the mean pixel value within each aperture as well as the average mean over all apertures and, finally, computing the standard deviation of the mean pixel values in those individual apertures. Map making uncertainties are derived from the error map, which is produced during the data reduction procedure. Specific uncertainties in map making are determined from this error map. The total uncertainty on the flux value in a pixel is calculated as the square root of the sum of the three squared error contributions. Calibrations and background uncertainties are summarized in Table 2.

The noise level in PACS spectroscopy observations is determined from the uncertainty in the integrated intensity map, calculated from the formula

$$\Delta I = [\Delta v \sigma \sqrt{N_{\text{line}}}]\sqrt{1 + \frac{N_{\text{line}}}{N_{\text{base}}}}, \qquad (1)$$

where Δv corresponds to the channel width in km s^{-1}, σ is the uncertainty in K and N_{line} and N_{base} represent the total number of channels covering the spectral line and the channels used for the baseline fitting, respectively. A 1σ uncertainty value is estimated from taking the mean over 15 random apertures in this uncertainty map (see Table 1).

2.5 JCMT observations and ancillary data

The JCMT observations of the ^{12}CO (3–2) transition (rest frequency 345.79 GHz) were obtained with the HARP-B instrument (Buckle et al. 2009) as part of project M10AC07 (PI: Tara Parkin) over eight nights in 2010 May, June and September, with a telescope

Table 1. The 1σ noise levels for the PACS spectroscopy observations.

Line	Rest wavelength	σ
	(μm)	(10^{-6} erg s^{-1} cm^{-2} sr^{-1})
[C II]	157.74	1.28
[O I] (centre)	63.18	5.50
[O I] (north)	63.18	7.06

beam size of 14.5 arcsec. We obtained a single map in jiggle-chop mode with a footprint of 2 × 2 arcmin^2 on the sky, and a total integration time of 1350 s for each of the 16 jiggle positions. The observations were carried out using beam-switching with a chop throw of 150 arcsec from the centre of NGC 205. We used the Auto-Correlation Spectrometer Imaging System as our backend receiver, and it was set to a bandwidth of 1 GHz with 2048 channels, resulting in a resolution of 0.43 km s^{-1}. The data were then reduced using the STARLINK[3] software package (Currie et al. 2008), maintained by the Joint Astronomy Centre. For a full description of our data reduction and map making methods, see Warren et al. (2010) and Parkin et al. (2012).

We obtained raw Multiband Imaging Photometer (MIPS) data for NGC 205 from the *Spitzer* archive, which were reprocessed according to the procedure outlined in Bendo, Galliano & Madden (2012b). An H I map for NGC 205 obtained from VLA observations (Young & Lo 1997) was kindly provided to us by Lisa Young.

3 RESULTS

3.1 Distribution of gas and dust in the ISM of NGC 205

Fig. 2 displays the *Herschel* maps for NGC 205 in the PACS 70, 100, 160 μm and SPIRE 250, 350 and 500 μm wavebands. In all bands, we are able to distinguish three dominant emission regions (north, central and south), which were first identified using MIPS data by Marleau et al. (2006). A substantial amount of dust also resides in between those three distinctive emission regions. Towards the south-east of NGC 205 there is also an indication for a tentative detection of a colder dust component in the SPIRE maps (see the red, dashed ellipse in Fig. 2). The detection is below the 3σ level, but it coincides with an optical tidal tail reported in Saviane, Monaco & Hallas (2010). However, we cannot rule out the possibility that the faint blob corresponds to foreground Galactic cirrus emission similar to the emission identified in the surroundings of M81 (Davies et al. 2010; Sollima et al. 2010) or to emission originating from one or multiple background sources.

When comparing the H I, H$_2$ and dust distribution in NGC 205 (see Fig. 3), we find a remarkable correspondence between the peaks in H I and H$_2$ [as derived from the CO (3–2) observations; see Section 3.4] column density and dust emission. This seems to imply that the dust component in NGC 205 is well mixed with the atomic and molecular gas at the observed spatial scales of ∼100 pc for SPIRE. While a significant part of the atomic gas resides in the area south of the galaxy's centre (see Fig. 3), current CO observations only cover most of the northern part of the galaxy [Johnson & Gottesman 1983; Young & Lo 1997; Welch et al. 1998; JCMT CO
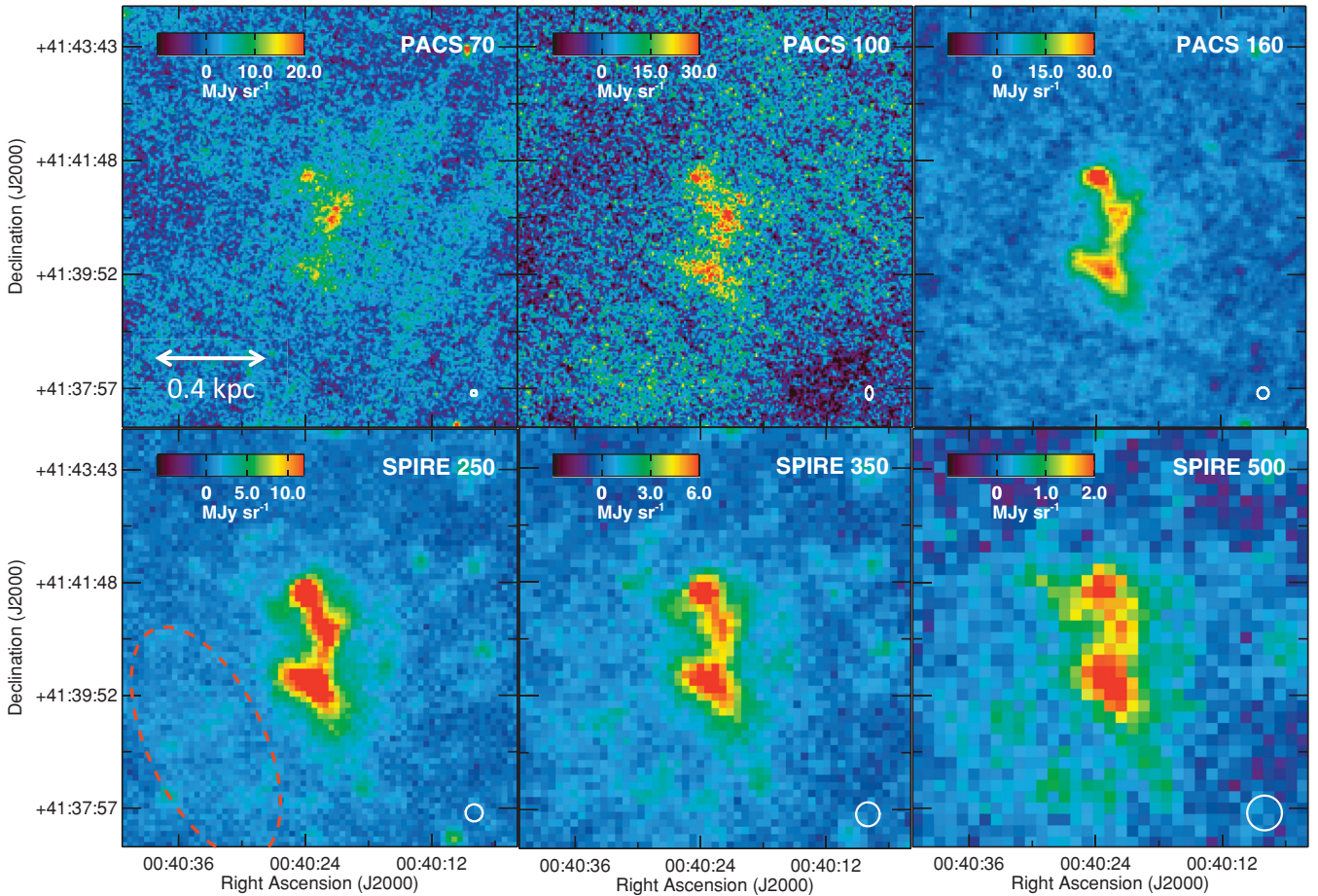
Figure 2. An overview of the *Herschel* maps. From left to right: PACS 70, 100, 160 μm (first row) and SPIRE 250, 350, 500 μm (second row). The displayed maps cover an area of 8.0×6.5 arcmin^2, with north up and east to the left. Besides the PACS 70 μm (VNGS) and PACS 100 μm (HELGA) maps, all images in the other bands were produced using both VNGS and HELGA observations. The FWHM of the PSF is indicated as a white circle in the lower left corner of each image. The red dashed line indicates the area where there is an indication for a tentative detection of a colder dust component.

(3–2) map from this work] and a minor part in the south of NGC 205 (Young & Lo 1996). This lack of data makes it difficult to draw conclusions about the correlation of the molecular gas component with the dust or H I gas in the southern area of NGC 205. At least for the northern part of NGC 205, it seems that also the molecular gas component correlates well with the H I gas and dust.

3.2 Global fluxes

Global fluxes in all wavebands were determined from summing over all pixels in the background-subtracted image with $>3\sigma$ detection in the SPIRE 250 μm image. Those global fluxes and the corresponding noise measurements (calibration uncertainty and random background noise) in each waveband are summarized in Table 2. Flux measurements have been updated to the last PACS and SPIRE calibration products, converted to the extended source calibration and colour corrected for each filter.

When comparing our fluxes at PACS 70 μm (2.2 ± 0.2 Jy) and PACS 160 μm (4.0 ± 0.3 Jy) to the MIPS fluxes at those overlapping wavelengths reported in Marleau et al. (2006) (MIPS 70 μm: 1.4 ± 0.3 Jy; MIPS 160 μm: 8.8 ± 4.7 Jy), a large discrepancy between PACS and MIPS fluxes is found. In view of this large difference, we determined MIPS fluxes (MIPS 70 μm: 1.3 ± 0.3 Jy; MIPS

160 μm: 4.6 ± 0.9 Jy) from our reprocessed archival MIPS data by summing over the same pixels (uncertainty values only refer to calibration uncertainties). To determine the corresponding PACS fluxes, the *Herschel* maps at 70 and 160 μm wavelengths were convolved with the appropriate kernels to match the elongated wings of the MIPS PSFs. The customized kernels were created following the procedure in Bendo et al. (2012a, see also Gordon et al. 2008). Summing the flux values for the same pixels, we find the corresponding flux measurements for PACS 70 μm (2.3 ± 0.2 Jy) and PACS 160 μm (3.8 ± 0.3 Jy). Upon comparison of the fluxes, we find a relatively good agreement between the PACS measurement and the flux determined from the archival MIPS image at 160 μm. The PACS 70 μm flux is sufficiently higher, which might either be a calibration issue or a dissimilarity in the background determination. We argue that the deviation from the MIPS 160 μm measurement reported in Marleau et al. (2006) is either due to a flux calibration issue or an overestimated aperture correction. Indeed, the flux calibration for MIPS (Gordon et al. 2007; Stansberry et al. 2007) was only finalized after the analysis in Marleau et al. (2006).

A similar comparison at 100 μm is possible between PACS and *IRAS* fluxes. Rice et al. (1988) report a total flux density of 3.78 ± 0.57 Jy for NGC 205, which agrees well with the flux density 3.6 ± 0.5 Jy determined from *Herschel* observations.
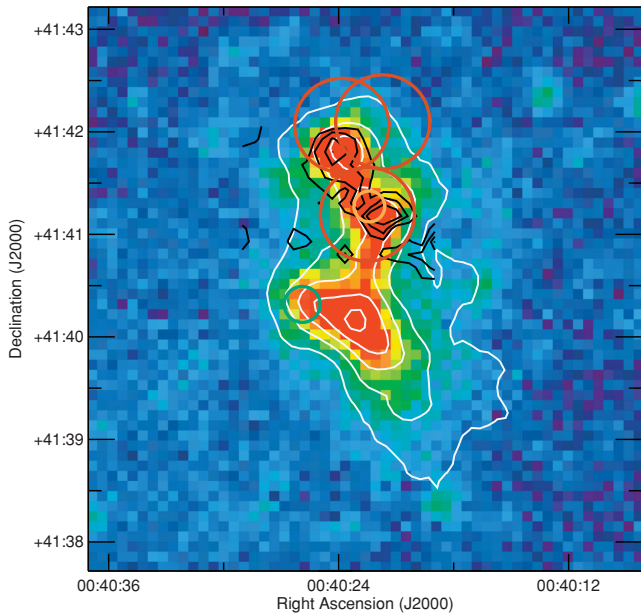
Figure 3. H I column density contours (white, solid line: Young & Lo 1997), H₂ column density contours [black, solid contours, derived from the JCMT CO (3–2) map], CO (1–0) pointings (red circles: Welch et al. 1998; green circle: Young & Lo 1996) and JCMT 1.1 mm 18 arcsec beam (yellow circle, Fich & Hodge 1991) overlaid on the SPIRE 250 μm image. The H I contours range from 2×10^{19} to 3.5×10^{20} cm⁻² in intervals of 6.6×10^{19} cm⁻², while the CO (3–2) contours represent an H₂ column density range $2.6 \times 10^{20} \leq N_{H_2} \leq 1.9 \times 10^{21}$ cm⁻² increased in steps of 3.3×10^{20} cm⁻².

Table 2. Global fluxes (F_ν) and contributions from the random background noise (σ_{back}) and the calibration uncertainty (σ_{cal}) are provided for every waveband. All tabulated fluxes have been multiplied by extended source calibration and filter colour correction factors.

Wavelength	F_ν	σ_{back}	σ_{cal}
(μm)	(mJy)	(μJy arcsec⁻²)	(per cent)
MIPS 24	98 ± 15		15^a
PACS 70	2204 ± 179	0.5	3
PACS 100	3565 ± 515	1.2	3
PACS 160	3912 ± 159	2.2	5
SPIRE 250	2623 ± 29	1.8	7
SPIRE 350	1302 ± 15	1.6	7
SPIRE 500	539 ± 9	2.3	7

^{a}The 15 per cent uncertainty on the MIPS 24 μm flux includes the uncertainties arising from calibration and background subtraction.

3.3 Calculation of the dust mass

3.3.1 SED fitting method

For the SED fitting procedure, we apply the DUSTEM code (Compiègne et al. 2011), which predicts the emission of dust grains given the strength of the interstellar radiation field (ISRF) and a certain composition of grain types, with a specific size distribution, optical and thermal dust properties. DUSTEM derives the local dust emissivity from computing explicitly the temperature distribution for every grain type of particular size and composition. For the analysis in this paper, we adopt two different dust compositions (Draine & Li 2007 and Compiègne et al. 2011), each containing polycyclic

aromatic hydrocarbons (PAHs) and amorphous silicate grains complemented with either graphite or amorphous carbon dust particles, respectively. The dust composition from Draine & Li (2007) corresponds to the typical dust mixture found in our own Galaxy. The amorphous carbonaceous grains are in the form of hydrogenated amorphous carbon, better known as a-C:H or HAC (Compiègne et al. 2011). The spectral shape of the ISRF is assumed to be the same as determined in the solar neighbourhood (Mathis, Mezger & Panagia 1983). Although the shape and hardness of the ISRF in low-metallicity dwarf galaxies might differ from the Galactic ISRF (Madden et al. 2006), altering the spectral shape of the ISRF will in particular influence the radiation of transiently heated PAHs and very small grains but has been shown to only affect the total dust mass estimate by a factor of <10 per cent (Galametz et al. 2009). Moreover, based on the number and spectral type of young massive stars in NGC 205, Young & Lo (1996) found an ultraviolet field corresponding well to the ISRF in the solar neighbourhood. Under these assumptions, we have only two free parameters: the dust mass M_d and the intensity of the ISRF X_{ISRF} relative to the Galactic ISRF.

During the SED fitting procedure, we explore a parameter grid in X_{ISRF} and dust mass by increasing them stepwise by a factor of 1.05. In order to facilitate the least-square fitting procedure, we construct a pre-calculated library of dust models in DUSTEM, each with a different scaling of the ISRF and dust mass. The model SED at those wavelengths is convolved with the response function of the filter band passes, to include the appropriate colour correction (pixel values were not colour corrected in this case). Finally, the model with the best-fitting parameters is determined from a least-square fitting routine. To estimate the uncertainties on the best-fitting parameters, we perform a bootstrapping procedure. Hereto, the same fitting routine is applied on a data set of 100 flux densities, randomly determined from a Gaussian distribution for which the maximum value and width are chosen to correspond to the observed fluxes and uncertainty values. The 1σ uncertainties on our best-fitting model parameters correspond to the 16 and 84 percentiles of this Gaussian distribution.

Since the primary goal of this analysis is quantifying the total dust content in NGC 205, we restrict our SED fitting procedure to the wavelength range from 24 to 500 μm. The spectral shape throughout this wavelength range is determined from the flux measurements in the six available *Herschel* wavebands (PACS 70, 100, 160 μm and SPIRE 250, 350, 500 μm) and the MIPS 24 μm flux. Prior to SED fitting, all images (*Herschel*+ancillary MIPS data) were convolved with the appropriate kernels, according to the procedure in Bendo et al. (2012a), to match the resolution of the 500 μm images. All images were also rebinned to the pixel scale (12 arcsec pixel⁻¹) of the 500 μm image.

3.3.2 Pixel-by-pixel fitting

Dust masses and ISRF scaling factors are computed from an SED fitting procedure to every pixel with fluxes in at least three different bands above the 3σ level to constrain the spectral shape of the energy distribution. In this way, we obtain 155 pixels with a sufficient signal-to-noise ratio level and avoid contribution from noisy pixels (in particular at 100 μm) to the SED fitting procedure, which might bias our estimate of the total dust mass. The uncertainties on the flux values in every pixel are calculated following the procedure outlined in Section 2.4.

Fig. 4 shows the maps with the best-fitting ISRF scaling factors (left) and dust column densities (right), determined from SED fitting
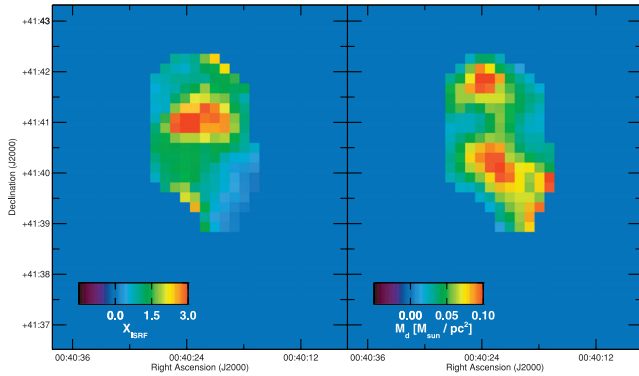
Figure 4. The $X_{\rm ISRF}$ (left-hand panel) and dust mass (right-hand panel) obtained from a multicomponent DustEm SED fitting procedure for every pixel with at least three detections above the 3σ level across the 24–500 μm wavelength range.

with the silicate+amorphous carbon dust composition (Compiègne et al. 2011). From those maps, we clearly note that the dust in the centre of NGC 205 has a higher temperature, while most of the dust mass resides in the northern and southern regions of NGC 205, corresponding to peaks in the H I+H$_2$ and H I column density, respectively. For the three distinctive dust emission regions in NGC 205, the northern and southern areas are brighter because of the large amounts of dust residing in these areas, while the dust grains in the central region emit more prominently because they are exposed to a stronger ISRF. Also outside these three emission regions, a substantial amount of dust is found to be present in the galaxy.

The total dust mass in NGC 205 is determined by adding the dust masses in all pixels, resulting in $M_{\rm d} \sim 1.8 \times 10^4\,{\rm M_\odot}$. An estimate for the average strength of the ISRF is calculated as the median of the values for $X_{\rm ISRF}$ in all pixels. This median value of $X_{\rm ISRF} \sim 1.13$ is translated into a large grain dust temperature $T_{\rm d} \sim 17.8$ K by averaging over all mean temperatures for grains with sizes between 4×10^{-3} and 2 μm for this specific strength of the ISRF. When repeating the SED fitting procedure with a silicate+graphite dust composition (Draine & Li 2007), we find values for the dust mass ($M_{\rm d} \sim 1.1 \times 10^4\,{\rm M_\odot}$) and the median value of the scaling factor $X_{\rm ISRF} \sim 3.12$ (or $T_{\rm d} \sim 21.2$ K) consistent with the results obtained for a silicate+amorphous carbon dust composition within the uncertainties of the SED fitting procedure. The fitting results for both dust compositions are summarized in Table 3. To check whether

our results are hampered by the resolution in the SPIRE 500 μm waveband ($\sim$36 arcsec), we perform the same pixel-by-pixel SED fitting procedure at a resolution of the SPIRE 350 μm waveband ($\sim$24.5 arcsec). Whereas SED fitting on higher resolution data has shown to probe a more massive dust reservoir in the Large and Small Magellanic Clouds (LMC and SMC, respectively; Galliano et al. 2011), we find best-fitting values for the average scaling factor $X_{\rm ISRF} \sim 0.61^{+0.31}_{-0.31}$ and the total dust mass $M_{\rm d} \sim 0.9^{+0.5}_{-0.5} \times 10^4\,{\rm M_\odot}$. Since the dust mass is somewhat lower than the results obtained from the SED fit with the 500 μm measurement, we conclude that a gain in resolution does not better trace the dust content in NGC 205. On the contrary, including the 500 μm data in the SED fit results in a more massive dust component at a colder temperature in the outer regions of NGC 205.

An SED fitting procedure for the global fluxes was performed as well, giving similar results as for the pixel-by-pixel dust masses and $X_{\rm ISRF}$ factors (see Table 3). Fig. 5 displays the best-fitting DUSTEM model for the silicate+amorphous carbon dust composition overlaid with the global *Herschel* fluxes and other data from the literature.

3.3.3 Submm/mm excess

The dust masses obtained from our *Herschel* observations ($M_{\rm d} \sim 1.1$–$1.8 \times 10^4\,{\rm M_\odot}$) are comparable to the dust masses derived from the MIPS observations ($M_{\rm d} \sim 3 \times 10^4\,{\rm M_\odot}$) within the uncertainties of the observations and fitting procedure, but more than one order of magnitude lower than the predicted dust mass ($M_{\rm d} \sim 5 \times 10^5\,{\rm M_\odot}$) at a temperature of $\sim$12 K based on mm+*Spitzer* observations (Marleau et al. 2006). Since the strength of the ISRF and therefore the heating of the dust grains is variable throughout the plane of the galaxy (see Fig. 4, left-hand panel), we calculate an upper limit for the dust mass at a dust temperature of $T_{\rm d} \sim 12$ K by scaling the SED until fitting the upper limit of the 500 μm flux measurement ($F_\nu \sim 612$ mJy). We derive an upper mass limit $M_{\rm d} < 4.9 \times 10^4\,{\rm M_\odot}$ for the cold dust reservoir ($T_{\rm d} \sim 12$ K). Therefore, our *Herschel* observations do not seem to support the presence of a massive cold dust component, implying that the mm flux is unlikely to originate from a cold dust reservoir.

With an upper limit of 0.06 mJy at 21 cm (Lucero & Young 2007) and the absence of emission-lines characteristic for low-ionization nuclear emission-line region (LINER) or Seyfert galaxies (Martins et al. 2012), the JCMT 1.1 mm flux measured by Fich & Hodge (1991) is unlikely to be caused by synchrotron emission from either supernova remnants (SNRs) or an active galactic nucleus (AGN) like nucleus. Also the contribution from CO (2–1) line emission seems unable to account for the high mm measurement. Indeed, based on the JCMT CO (2–1) line intensity (0.43 K km s^{-1}) for the inner region (Welch et al. 1998), we derive a flux density of 0.724 Jy at 1.3 mm. Relying on the narrow CO (2–1) linewidth (13 km s^{-1} or 10 MHz) and the bandwidth of the IRAM UKT14 receiver (74 GHz), a contribution from CO (2–1) line emission to the 1.1 mm continuum observations is found to be negligible. This implies that other explanations (calibration issues, background source, bad weather conditions) need to be invoked to explain the high 1.1 mm flux in the centre of NGC 205.

Also *Herschel* observations at 500 μm do not show any indication for excess emission at submm or mm wavelengths, reminiscent of the submm excess observed in many star-forming dwarf galaxies and blue compact dwarfs (Galliano et al. 2003; Dumke, Krause & Wielebinski 2004; Galametz et al. 2009, 2010, 2011; Grossi et al.
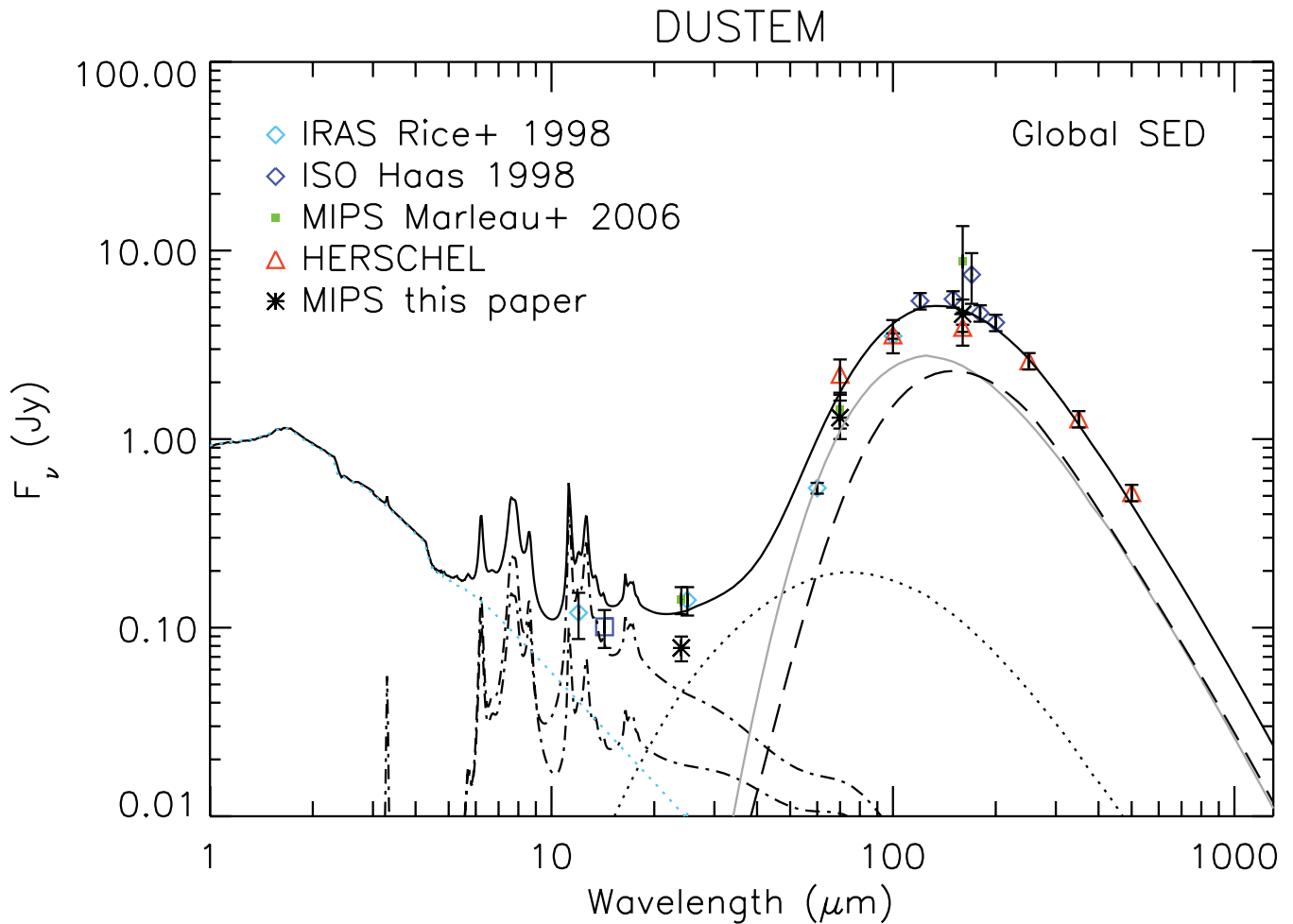
Table 3. Overview of the parameters (scaling factor for the ISRF $X_{\rm ISRF}$, dust mass $M_{\rm d}$) for the best-fitting DustEm model, either with a silicate+amorphous carbon or silicate+graphite dust composition, determined from a pixel-by-pixel or global SED fit. The temperature estimate is obtained by taking the average over all mean temperatures for dust particles with sizes between 4×10^{-3} and 2 μm.

Silicate/am. carbon	$X_{\rm ISRF}$	$T_{\rm d}$ (K)	$M_{\rm d}$ (M$_\odot$)
Pixel-by-pixel	$1.13^{+0.07}_{-0.07}$	$17.8^{+0.2}_{-0.1}$	$1.8^{+0.1}_{-0.1} \times 10^4$
Global	$2.74^{+0.42}_{-0.58}$	$20.7^{+0.5}_{-0.8}$	$1.1^{+0.1}_{-0.1} \times 10^4$
Silicate/graphite	$X_{\rm ISRF}$	$T_{\rm d}$ (K)	$M_{\rm d}$ (M$_\odot$)
Pixel-by-pixel	$3.12^{+0.19}_{-0.19}$	$21.2^{+0.2}_{-0.3}$	$1.1^{+0.1}_{-0.1} \times 10^4$
Global	$3.74^{+0.10}_{-1.37}$	$21.8^{+0.1}_{-1.6}$	$1.0^{+0.3}_{-0.1} \times 10^4$

DUSTEM

Figure 5. The SED for the best-fitting DustEm model ($X_{ISRF} = 2.74$ or $T_d \sim 20.7$ K, $M_d \sim 1.1 \times 10^4$ M$_\odot$) with a silicate+amorphous carbon dust composition (black, solid line), overlaid with the measured MIPS 24 μm, PACS 70, 100, 160 μm and SPIRE 250, 350 and 500 μm flux densities. Also the other flux densities from the literature are indicated. The dot–dashed, dotted, grey and dashed lines correspond to the PAH dust mixtures, small and large amorphous carbon and silicate dust grains, respectively. Since the SED fitting procedure with the silicate+graphite dust composition gave very similar results and uncertainties, the plot with this SED model is not explicitly shown here. Also a stellar component for NGC 205, parametrized as a Maraston (1998, 2005) single stellar population with an age of 13 Gyr and a metallicity of $Z = 0.002$ (Bertola et al. 1995) and modelled as a Sérsic profile of index $n = 1$ and effective radius 130 arcsec (De Rijcke et al. 2006), was included on the SED fit, to allow a comparison of our SED model to observations at NIR/MIR wavelengths (blue dotted line).

2010; O'Halloran et al. 2010). In some cases, the observed excess even extends up to mm and cm wavelengths, such as observed in the LMC and SMC (Bot et al. 2010; Israel et al. 2010; Meixner et al. 2010; Planck Collaboration et al. 2011). Several reasons have been invoked to account for this excess emission in the submm/mm wavebands. Either large amounts of very cold dust (e.g. Galliano et al. 2003, 2005; Galametz et al. 2009; O'Halloran et al. 2010), dust grains with optical properties diverging from the typical Galactic dust characteristics (e.g. Lisenfeld et al. 2002; Meny et al. 2007) or spinning dust grains (e.g. Bot et al. 2010; Planck Collaboration et al. 2011) are thought to be responsible for the excess emission. The fact that our SED model can account for the observed 500 μm emission in NGC 205 is interesting, because it is in contrast with the submm excess observed in several other low-metallicity dwarf galaxies. This might be an indication for different ISM properties and star-forming conditions in this early-type dwarf galaxy, compared to the typical star-forming dwarfs revealing an excess submm emission. However, an excess in wavebands longwards of 500 μm (see also Galametz et al. 2011) cannot be ruled out based on the currently available data set for NGC 205.

3.4 Gas mass

3.4.1 JCMT CO (3–2) observations

In view of the limited coverage of previous CO (1–0) and CO (2–1) observations with only a few pointings across the galaxy, we derive a molecular gas mass estimate for NGC 205 from a CO (3–2) map covering a larger part of the galaxy, however still only probing the H$_2$ gas in the northern region of the galaxy (see Fig. 3).

For all pixels with detections $>3\sigma$, the integrated CO (3–2) line intensity is converted to an H$_2$ column density according to the formula

$$N_{H_2} = \frac{X_{CO} I_{CO(3-2)}}{\eta_{mb} \left(\frac{I_{CO(3-2)}}{I_{CO(1-0)}} \right)}, \tag{2}$$

where $I_{CO(3-2)}$ is the total integrated line intensity expressed in units of K km s^{-1}. The scaling factor to convert an antenna temperature $T_A^\star$ into a main beam temperature T_{mb} at the JCMT is $\eta_{mb} = 0.6$. We assume a value of ~ 0.3 for the CO (3–2)-to-CO (1–0) line intensity ratio corresponding to the typical ratios found in the diffuse ISM

of other nearby galaxies (Wilson et al. 2009). Since we derive a line ratio of ∼0.34 for the central pointing reported in Welch et al. (1998), we argue that this ratio serves as a good approximation for the entire CO (3–2) emitting region. The same X_{CO} conversion factor $[6.6 \times 10^{20} \, \text{cm}^{-2} \, (\text{K km s}^{-1})^{-1}]$ as introduced in Section 1.2 is applied here. The total molecular gas mass is derived from the column density following the equation

$$M_{H_2} = A N_{H_2} m_{H_2}, \tag{3}$$

where A represents the surface of the CO (3–2) emitting region and m_{H_2} is the mass of a molecular hydrogen atom. Inserting the correct values in equation (3) results in an estimate for the total molecular gas mass $M_{H_2} \sim 1.3 \times 10^5 \, M_\odot$. Considering that this value is a factor of ∼5 lower than the $M_{H_2} \sim 6.9 \times 10^5 \, M_\odot$ inferred from CO (1–0) detections, we argue that most of the H$_2$ in NGC 205 resides in regions of colder temperature ($T \leq T_{\text{crit,CO(3-2)}} \sim 33 \, \text{K}$) and/or lower density ($n \leq n_{\text{crit,CO(3-2)}} \sim 2 \times 10^4 \, \text{cm}^{-3}$).

3.4.2 PACS spectroscopy observations

Relying on the low metal abundance of the ISM in the inner regions of NGC 205, there might be a significant fraction of molecular gas in NGC 205 which remains undetected by current CO observa-

tions, since CO is often a poor diagnostic of the H$_2$ content in low abundance environments exposed to hard radiation fields. Based on the high values for the $L_{[C\,II]}$-to-L_{CO} ratio found in several low-metallicity dwarf galaxies (e.g. Madden 2000; Cormier et al. 2010), [C II] is often claimed to be a better tracer for the molecular gas in such environments. Also the [O I] fine-structure line, which is considered an important coolant of the neutral gas together with [C II], can be used as an alternative probe for the molecular gas in a low-metallicity ISM (e.g. Tielens & Hollenbach 1985). Although both [C II] and [O I] are considered good tracers of molecular gas in a metal-poor ISM, the interpretation of their line fluxes is hampered by a lack of knowledge about the exact origin of the line emission from within a galaxy. [C II] emission is thought to arise either from the ionized (H II regions) or the neutral [photodissociation regions (PDRs)] medium, while [O I] emission originates mainly from the neutral ISM. In those neutral PDRs, the [C II] line provides cooling for gas clouds with a moderate density ($n_{H_2} < 10^4 \, \text{cm}^{-3}$), while the [O I] line cools the higher density regions.

From our PACS spectroscopy observations, we detected [C II] line emission in the centre of NGC 205 (see Fig. 6, left-hand panel), while the [O I] line was not detected in either of the two covered regions in NGC 205 (see Fig. 7). The faint [C II] emission in NGC 205 originates mainly from the nuclear region, with the peak

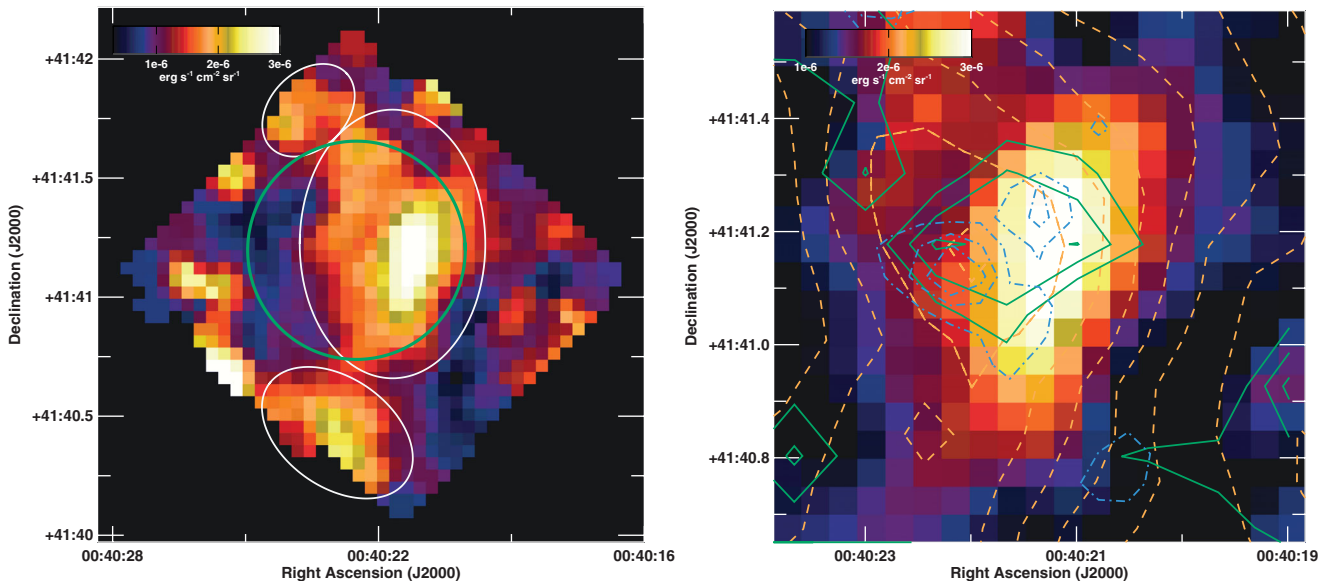**Figure 6.** Left: PACS [C II] map of NGC 205. The elliptical apertures for photometry are indicated as white circles. The CO (1–0) pointing reported in Welch et al. (1998) covering the centre of NGC 205 as well as the [C II] intensity peak is colour coded in green. Right: zoom on the central bright region in the [C II] map, overlaid with contours of MIPS 24 μm surface brightnesses (blue, dot–dashed curves) and H I and CO (3–2) column densities (yellow, dashed and green solid lines, respectively). The H I contours range from 2×10^{19} to $2.6 \times 10^{20} \, \text{cm}^{-2}$ in intervals of $4 \times 10^{19} \, \text{cm}^{-2}$, while the CO (3–2) contours represent an H$_2$ column density range $1.83 \times 10^{20} \leq N_{H_2} \leq 1.28 \times 10^{21} \, \text{cm}^{-2}$ increased in steps of $2.75 \times 10^{20} \, \text{cm}^{-2}$. The contours representing the MIPS 24 μm surface brightnesses range from 0.68 to 2 MJy sr^{-1}, stepwise increased by 0.33 MJy sr^{-1}.
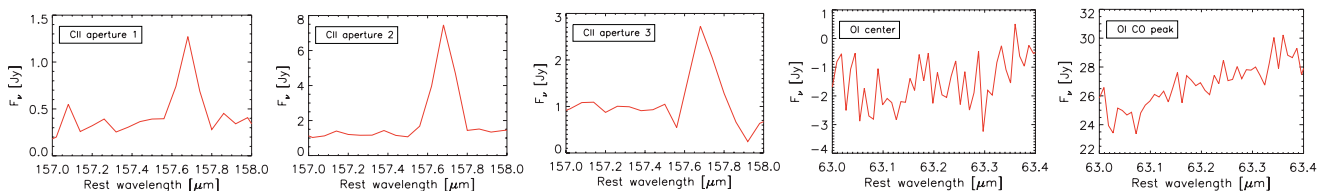

Figure 7. PACS spectral line plots. First three panels show the [C II] line emission summed over the individual apertures shown in Fig. 6 and described in Table 4, respectively. The last two panels show the non-detection of the [O I] line, with the emission added up within the observed regions covering the centre and the CO peak in NGC 205, respectively.

intensity residing from a dust cloud west of the nucleus. From the gas and dust contours in Fig. 6 (right-hand panel), it becomes evident that the brightest [C II] emission region is located at the boundary of the most massive H I and molecular clouds in the centre of NGC 205. The spatial correlation with the CO reservoir in the centre of NGC 205 and the surrounding star formation regions (see contours of hot dust emission from MIPS 24 μm data, Fig. 6, right-hand panel, blue, dot–dashed curves) suggests that the [C II] emission in NGC 205 originates from PDRs in the outer layers of molecular cloud structures. Although the [C II] emission in galaxies might have a significant contribution from ionized media, the unavailability of ionized gas tracers (e.g. [N II], [O III]) impedes a direct quantification of the [C II] emission from ionized regions. The non-detection of Hα line emission (Young & Lo 1997) seems to point towards a low fraction of ionized gas in the ISM of NGC 205.

To determine the intensity of the [C II] line emission in NGC 205, we performed aperture photometry within ellipses matching the shape of prominent [C II] emission regions in NGC 205 (see Fig. 6, left-hand panel). The spectral line emission within each emission region is shown in Fig. 7 (first three panels). The fluxes within those three apertures are summarized in Table 4. From equation (1) in Madden et al. (1993), we can derive the column density of atomic hydrogen, when adopting a C^+ abundance per hydrogen atom of $X_{C^+} = 1.4 \times 10^{-4}$ (Savage & Sembach 1996) and $n_{crit} \sim 2.7 \times 10^3$ cm^{-3}. When assuming $X_{ISRF} \sim 3$ (or thus $G_0 \sim 3$) for the strength of the ISRF field (see Section 3.3) and an average density $n_H \sim 10^4$ cm^{-3}, we estimate a surface density temperature of $T \sim 40$ K from the PDR models in Kaufman et al. (1999). Inserting those values in equation (1) from Madden et al. (1993), we obtain average column densities for the three apertures within the range $2.2 \times 10^{19} \leq N_H \leq 3.7 \times 10^{19}$ cm^{-2}. Summing over all three apertures, the total atomic gas mass for the [C II] emitting regions in NGC 205 is derived to be $M_g \sim 1.54 \times 10^4$ M$_\odot$. Since this value is negligible compared to the total gas mass $M_g \sim 6.9 \times 10^6$ M$_\odot$ derived from CO (1–0) observations (see Section 1.2), we conclude that the molecular gas reservoir is probably well traced by the CO lines in the low-metallicity ISM of NGC 205. This argument is furthermore supported by the relatively low $L_{[C II]}$-to-$L_{CO(1-0)}$ line intensity ratio ∼1850 within the central CO (1–0) pointing from Welch et al. (1998) (see green aperture overlaid on Fig. 6). This line intensity ratio is substantially lower than the values observed in star-forming dwarf galaxies ranging from 4000 to 80 000 (Madden 2000; Cormier et al. 2010).

Based on PDR models for values $X_{ISRF} \sim 3$ and $n_H \sim 10^4$ cm^{-3} in the centre of NGC 205, we would expect [C II] line intensities of a few 10^{-6} erg cm^{-2} s^{-1} sr^{-1} and $L_{[O I]}$-to-$L_{[C II]}$ line intensity ratios close to 0.5 (see figs 3 and 4 from Kaufman et al. 1999). With a peak [C II] line intensity of 3×10^{-6} erg cm^{-2} s^{-1} sr^{-1} and an upper limit of $L_{[O I]}$-to-$L_{[C II]} < 1.75$, the observed [C II] line emission in the centre of NGC 205 is in agreement with PDR models.

The lack of any bright [C II] emission from other regions in NGC 205 might be an indication for the strength of the radiation field being insufficient to photodissociate CO. This argument is supported by the pixel-by-pixel analysis in Section 3.3.2, which indicates the stronger radiation field in the brightest [C II] region compared to the rest of the galaxy (see Fig. 4, left-hand panel). Alternatively, a large reservoirs of photodissociated CO molecules might be present in the outer layers of gas clouds, where a deficiency of ionizing photons might impede the formation of C^+ atoms. A lack of ionizing photons is also supported by the non-detection of Hα in this galaxy (Young & Lo 1997). According to this latter scenario, we would expect the majority of dissociated carbon to be locked in [C I] rather than C^+.

4 DISCUSSION

4.1 Missing ISM mass problem: revised

From our *Herschel* observations of the dust continuum and far-infrared (FIR) fine structure lines [C II] and [O I] and JCMT CO (3–2) data, we are able to revisit the missing ISM mass problem in NGC 205. We estimate an atomic gas mass of 1.54×10^4 M$_\odot$ associated with the [C II] emitting PDRs in NGC 205. From the CO (3–2) emitting regions in the northern part of NGC 205, we could derive a molecular gas mass of $M_{H_2} \sim 1.3 \times 10^5$ M$_\odot$. In comparison with the $M_{H_2} \sim 6.9 \times 10^5$ M$_\odot$ obtained from pointed CO (1–0) observations (Welch et al. 1998) covering the main CO (1–0) emission regions in the north of the galaxy, our CO (3–2) measurements indicate a low fraction of dense molecular gas in the diffuse ISM of NGC 205, where star formation is currently only occurring spontaneously in localized dense clouds. Including H I observations (4.0×10^5 M$_\odot$) and scaling the sum of the molecular and atomic hydrogen mass by a factor of ∼1.4 to include heavier elements, we obtain a total gas mass of $M_g \sim 0.7$–1.5×10^6 M$_\odot$ from CO (3–2) or CO (1–0) observations, respectively.

Alternatively, we probed the ISM content through the galaxy's dust continuum emission. This approach avoids introducing uncertainty factors arising from the X_{CO} conversion factor, but additional errors on the gas mass estimates result from the SED fitting procedure to calculate the dust mass and, even more importantly, the assumption on the value for the gas-to-dust ratio. Since it has been shown that the gas-to-dust ratio in metal-poor galaxies deviates from the Galactic ratio (∼160; Zubko, Dwek & Arendt 2004), a gas-to-dust fraction of ∼400 (Galliano, Dwek & Chanial 2008) is considered more realistic for the central ISM in NGC 205 in view of the recent star formation episode occurring in those inner regions. This value is obtained from an extrapolation of the dust evolution model in Galliano et al. (2008), when assuming little or no dust destruction and a first-order trend of the gas-to-dust ratio with metallicity ($Z \sim 0.3\,Z_\odot$). Relying on this gas-to-dust ratio of ∼400, the total dust mass detected from our *Herschel* observations corresponds to a gas mass $M_g = \sim 4$–7×10^6 M$_\odot$.

Upon comparison with the theoretical gas content in the range [1.3×10^7 M$_\odot$, 4.8×10^8 M$_\odot$] (see Section 1.1), gas mass estimates from either dust continuum (4–7 $\times 10^6$ M$_\odot$) or H I+CO (1–0)+[C II] (1.5×10^6 M$_\odot$) observations both confirm the missing ISM mass problem in NGC 205. The lower ISM mass inferred from direct gas observations (1.5×10^6 M$_\odot$) in comparison with the indirect gas estimates from dust continuum observations (4–7 $\times 10^6$ M$_\odot$) most likely results from the poor coverage of molecular

Table 4. [C II] line measurements within the elliptical apertures overlaid on the [C II] map in Fig. 6.

Aperture	RA (°)	Dec. (°)	a (arcsec)	b (arcsec)
1	10.095 534	41.673 843	21.20	13.76
2	10.090 351	41.687 053	33.84	23.45
3	10.098 251	41.696 41	13.39	9.65

Aperture	F_ν (10^{-14} erg s^{-1} cm^{-2})	M_{H_2} (M$_\odot$)
1	1.06 ± 0.25	1.26×10^3
2	9.91 ± 0.52	11.83×10^3
3	3.06 ± 0.56	2.27×10^3

gas tracers in NGC 205 and/or the uncertainty on the assumed gas-to-dust fraction (i.e. a gas-to-dust ratio closer to the Galactic value would bring the ISM masses inferred from H I+CO (1–0)+[C II] and dust continuum observations in better agreement). With the JCMT CO (3–2) and previous CO (1–0) and CO (2–1) observations mainly covering the northern part of the galaxy, the lack of knowledge about the molecular gas content for a large southern region in NGC 205, where the H I emission dominates, prevents us from determining the entire molecular gas content. If we assume a similar molecular-to-atomic gas mass ratio for the southern part of NGC 205 as observed in the northern part, the gas component in NGC 205 could be twice as massive than measured by current CO observations. The observed peak in H I (4×10^{20} cm^{-2} or 3.2 M$_\odot$ pc^{-2}) and dust (0.1 M$_\odot$ pc^{-2}) column density would imply an H I-to-dust ratio of ~ 32 in the south of NGC 205. However, a more realistic gas-to-dust ratio would require a large molecular gas reservoir residing in those southern areas. This argumentation is also confirmed by the H$_2$ column densities of 1.8 and 2.4×10^{20} cm^{-2} measured from two JCMT CO (2–1) pointings near the southern peak in H I, when assuming a CO (2–1)-to-CO (1–0) line ratio of $\sim 0.9 \pm 0.2$ as found by Young & Lo (1996) in a spatially resolved molecular cloud.

In addition to this unexplored molecular gas reservoir in the southern part of the galaxy, a substantial fraction of the gas component might remain undetected by current observations, either because a fraction of the gas is locked in hot X-ray or ionized gas haloes (similar to the heated gas returned by evolved stars in giant massive ellipticals) and/or the present molecular gas is traced neither by CO nor by [C II] molecules. Alternatively, we could invoke an internal/environmental mechanism solely removing the gas from NGC 205 and leaving the dust unharmed to explain the higher gas masses inferred from dust continuum observations. In view of the good correlation found for the gas and dust component, there is, however, no reason to assume a higher inertia for the dust and thus to imply that gas particles are more easily transported out of the gravitationally bound regions in NGC 205.

In the next paragraphs, we discuss possible explanations for the inconsistency between the observed ISM content (either from H I+CO (1–0)+[C II] or dust continuum observations) in NGC 205 and theoretical predictions, such as non-standard conditions for the SFE or initial mass function (IMF) or environmental processes able to remove part of the ISM during the last episode of star formation in NGC 205.

4.2 Explaining the inconsistency regarding the ISM mass

4.2.1 Non-standard conditions

Non-standard conditions such as a top-heavy IMF (more massive stars are produced, requiring less input gas mass) or a higher SFE (>10 per cent of the gas is converted into stars) could be invoked to explain the missing ISM in NGC 205.

Harmonizing the observed ISM content with the theoretical predictions would require an IMF deviating significantly from the general assumptions and/or an increase in the SFE from 10 per cent to at least 65 per cent. Although such a top-heavy IMF or increased SFE was thought to be present in some ultraluminous infrared galaxies (ULIRGS) or starbursts (e.g. M82; Knapp et al. 1980), the non-standard conditions in those galaxies are owing to the presence of high-density gas, introducing a different mode of star formation (Daddi et al. 2010). With a star formation rate (SFR) $\sim 7.0 \times 10^{-4}$ M$_\odot$ yr^{-1} (Monaco et al. 2009) during the last starburst

episode, NGC 205 does not mimic the typical star formation activity (>10 M$_\odot$ yr^{-1}) in those starburst galaxies. Also under less extreme circumstances, local variations in the SFE (Boquien et al. 2011a) and perturbations at the upper mass end of the IMF (Meurer 2010) have been claimed. However, the latter IMF variations have been questioned on its turn invoking poor extinction corrections and a variable SFR in those galaxies (Boselli et al. 2009; Weisz et al. 2012). Relying on recent results from Martín-Manjón et al. (2012) and Boylan-Kolchin et al. (2012), finding no evidence for extreme star formation efficiencies in star-forming dwarf galaxies and therefore rather supporting a moderate SFE of 10–20 per cent or less, we argue that non-standard conditions (top-heavy IMF and/or increased SFE) are not likely to occur in NGC 205. and we should invoke efficient mechanisms of gas removal to explain the low observed gas content in NGC 205.

4.2.2 Supernova feedback

Feedback from supernovae (SNe; Dekel & Silk 1986; Babul & Rees 1992; De Young & Heckman 1994) or potentially an AGN are capable of removing a significant amount of gas from NGC 205. Relying on the absence of any LINER or Seyfert diagnostics (Ho, Filippenko & Sargent 1995), we argue that the effect of AGN feedback in NGC 205 is currently negligible. Based on the 3σ upper limit of 3.8×10^4 M$_\odot$ for the mass of the supermassive black hole in NGC 205 from studies of the stellar kinematics based on deep *HST* images (Valluri et al. 2005), we believe the role of an AGN was also limited throughout the recent history of NGC 205. On the contrary, SN feedback and/or stellar winds could be responsible for expelling gas from the central regions, during the last episode of star formation. Examining the effectiveness of Type II SN (SN II) feedback during the last episode of star formation, Welch et al. (1998) confirm that SN winds or blasts were capable of removing a significant amount of gas from the central regions of NGC 205. Indeed, applying the dwarf galaxy model for $M_{\text{galaxy}} \sim 10^9$ M$_\odot$ from De Young & Heckman (1994), a minimum energy of $\sim 10^{55} f_{\text{gas}}$ erg would be required to expel most of the gas from the inner regions. Following the burst mass $\sim 7 \times 10^5$ M$_\odot$ reported in Wilcots et al. (1990), the gas fraction is found to be $f_{\text{gas}} \sim 0.007$, when assuming a 10 per cent SFE. This would require an energy of at least 7×10^{52} erg to remove gas. This level is easily achieved with the energy $\sim 6 \times 10^{54}$ erg released by the SNe II associated with the last burst (Welch et al. 1998). Keeping in mind the clumpy gas distribution and the offset of the local H I column density peaks from the locations of young stars (Young & Lo 1997) in addition to those theoretical arguments, we argue that both SN feedback and/or stellar winds have likely disturbed the ISM of NGC 205. Energy feedback from supernovae has furthermore been proven to have an important share in the formation of dwarf spheroidal systems (Kormendy et al. 2009).

Despite theoretical arguments supporting a history of violent SN explosions, a previous attempt to detect SNRs in NGC 205 failed ($F_\nu < 0.06$ mJy; Lucero & Young 2007). Relying on the low radio continuum detection rate for low surface brightness dwarfs (Hoeppe et al. 1994; Lucero & Young 2007), it might not be surprising that the detection of SNRs at 20 cm was unsuccessful. The majority of the 20 cm emission is thought to arise from synchrotron emission originating from electrons accelerated in the expanding shells of Type II and Type Ib SNRs. Due to the increased cosmic ray diffusion time-scales (Klein et al. 1992; Murphy et al. 2006; i.e. electrons are escaping more easily from the ISM) for galaxies with a low star formation activity (SFR ≤ 0.2 M$_\odot$ yr^{-1}), those objects become

radio quiet in short time-scales. Although violent SN explosions might have occurred in the past, the associated radio emission is likely smoothed out in the low potential well of NGC 205. Also in other wavelength domains, the detection of any SNRs will be challenging. While the star formation is known to be active up to at least 60 Myr ago, a typical age $\sim$10 Myr for an SN II progenitor and an SNR lifetime $\sim$25 000 yr imply that it is difficult to detect any remaining evidence of SNRs in NGC 205.

4.2.3 Environmental interactions

Galaxy harassment (Moore et al. 1996), starvation (Larson, Tinsley & Caldwell 1980) and viscous stripping (Nulsen 1982) are important transformation processes for galaxies in clusters, whereas tidal stirring (Mayer et al. 2001) and galaxy threshing (Bekki, Couch & Drinkwater 2001) are considered responsible for the formation of dwarf spheroidals and ultracompact dwarfs in the low-density environment of groups. For the formation of NGC 205, a combination of ram pressure and tidal stripping would be more likely since those processes are capable of transforming gas-rich dwarf galaxies into dwarfs with a blue central core when passing through the halo of a galaxy of the same size as the Milky Way (Mayer et al. 2006). Tidal or gravitational interactions are also considered to be the main formation mechanism for spheroidal and lens-shaped galaxies in groups (Kormendy et al. 2009; Bekki & Couch 2011; Smith et al. 2012). In a similar fashion, ram pressure stripping is found to form dEs with blue nuclei in the Virgo cluster (Boselli et al. 2008).

Several observations are indicative for the tidal influence of M31 on its companion NGC 205: a twist in the elliptical isophotes (Hodge 1973; Choi, Guhathakurta & Johnston 2002), a stellar arc of blue metal-poor red giant branch stars north-west of M31 (Ibata et al. 2001; McConnachie et al. 2004), a tidal debris of C stars to the west of NGC 205 (Demers, Battinelli & Letarte 2003), a stripped H I cloud 25 arcmin south-west of NGC 205 which overlaps in velocity with the galaxy (Thilker et al. 2004), peculiar H I morphology and kinematics (Young & Lo 1997), stars moving in the opposite direction with respect to the rotation of the main stellar body (De Rijcke et al. 2006; Geha et al. 2006) and an optical tidal tail extending at least 17 arcmin southwards from the galaxy's centre (Saviane et al. 2010). This latter stellar tail coincides with the tentative dust tail detected in our SPIRE data (see Section 3.1) and, thus, might be an indication for the removal of dust from NGC 205 as a result from the tidal influence of M31. Besides the tidal features characterizing NGC 205, M31 is also affected by the tidal influence exerted by NGC 205. While the origin of two off-centre spiral rings is probably attributable to a head-on collision with M32 (Block et al. 2006), the warped structure in the outer H I disc of M31 (Sato & Sawa 1986) and a distortion of the spiral structure in the disc (Gordon et al. 2006) are likely caused to some extent by a two-body interaction between M31 and NGC 205.

Although those observations confirm the tidal influence of M31 on the outer regions of NGC 205, it does not provide an explanation for the removal of gas from the inner regions, where the last episode of star formation took place and we would expect to find the leftover gas reservoir. Hydrodynamical simulations suggest that the gaseous component might be disrupted and partly removed even within the tidal radius (4 arcmin; Geha et al. 2006) without any indications for stellar bridges and tails at these radii (Icke 1985), but whether it is the case for NGC 205 is difficult to inquire due to the uncertainties regarding its orbit around M31 (Howley et al. 2008). However,

in combination with SN feedback expelling the gas from the inner regions, tidal interactions might strip the expelled gas from the outer regions.

Whether or not responsible for the removal of gas from the inner regions, a tidal encounter with a companion closer than 100–200 kpc is able to trigger star formation through shocks in the disc of a typical dwarf galaxy when moving on a coplanar prograde orbit (Brosch, Almoznino & Heller 2004). With a line-of-sight distance between the Andromeda galaxy and NGC 205 of $\sim$39 kpc (McConnachie et al. 2005) and the likely prograde trajectory of NGC 205 towards its parent galaxy, M31 (Geha et al. 2006; Howley et al. 2008), tidal interactions might have given the initial start for the last episode of star formation. Furthermore, the most recent episodes of star formation during the last gigayear seem correlated with the orbit about M31 (Davidge 2003), which provide additional evidence for the tidal triggering of star formation in NGC 205.

4.3 Comparison to other galaxies

Two other dwarf companions of M31, NGC 185 and 147, are thought to have a star formation history comparable to NGC 205 based on their nearly identical optical appearances (Holmberg diameters, $B - V$ colours, average surface brightnesses), mass-to-light ratios $(M/L)_B \sim 4\,M_\odot/L_{\odot,B}$ (De Rijcke et al. 2006) and specific frequencies of C stars (Davidge 2005), implying similar fractions of gas and dust which have been turned into stars in the past. Interestingly, both objects also feature a missing ISM mass problem (Sage, Welch & Mitchell 1998).

In correspondence to the missing ISM mass problem in NGC 205, tidal interactions and SN feedback are also believed to have influenced the ISM content in NGC 185 and 147. The tidal influence of M31 ($D = 785 \pm 25$ kpc; McConnachie et al. 2005) is considered negligible at distances of $D = 616 \pm 26$ and 675 ± 27 kpc (McConnachie et al. 2005) for NGC 185 and 147, respectively, compared to NGC 205 ($D = 824 \pm 27$ kpc; McConnachie et al. 2005). However, both galaxies are thought to form a gravitationally bound pair (van den Bergh 1998) and might have tidally interacted in the past. Aside from the possible occurrence of tidal interactions, indications for SNRs are found in NGC 185 (Gallagher, Hunter & Mould 1984; Young & Lo 1997; Lucero & Young 2007) and the current ISM content in this galaxy ($\sim$7.3 $\times$ 10^5 M$_\odot$) resembles the estimated mass returned to the ISM by planetary nebulae ($\sim$8.4 $\times$ 10^5 M$_\odot$; Sage et al. 1998). However, the lack of ISM in NGC 147 remains a puzzling feature in this evolutionary framework.

5 CONCLUSIONS

This work reports on *Herschel* dust continuum, [C II] and [O I] spectral line and JCMT CO (3–2) observations for NGC 205, the brightest early-type dwarf satellite of the Andromeda galaxy. While direct gas observations (H I+CO (1–0): 1.5 $\times$ 10^6 M$_\odot$) have proven to be inconsistent with theoretical predictions of the current gas content in NGC 205 ($>$10^7 M$_\odot$), we could revise the missing ISM mass problem based on new gas mass estimates (CO (3–2), [C II], [O I]) and an indirect measurement of the ISM content probed through *Herschel* dust continuum observations taken in the frame of the VNGS and HELGA projects.

SED fitting to the FIR/submm fluxes results in a total dust mass $M_d \sim 1.1$–1.8×10^4 M$_\odot$ at an average temperature $T_d \sim 18$–22 K. Based on *Herschel* data, we can also exclude the presence of a massive cold dust component ($M_d \sim 5 \times 10^5$ M$_\odot$, $T_d \sim 12$ K), which was suggested based on mm observations from the

inner 18.4 arcsec. When assuming a metal abundance $Z \sim 0.3\,Z_\odot$ and a corresponding gas-to-dust ratio ~ 400, a gas mass $M_g \sim 4$–$7 \times 10^6\,M_\odot$ is probed indirectly through *Herschel* dust continuum observations.

The non-detection of [O I] and the relatively low $L_{[\text{C II}]}$-to-$L_{\text{CO(1–0)}}$ line intensity ratio (~ 1850) imply that the molecular gas phase is well traced by CO molecules. From CO (3–2) observations of the northern part of the galaxy, we infer a new molecular gas mass estimate $M_{\text{H}_2} \sim 1.3 \times 10^5\,M_\odot$, implying that the molecular clouds in NGC 205 is mostly very diffuse.

New gas mass estimates from dust continuum and CO (3–2) line observations both confirm the missing ISM mass problem, i.e. an inconsistency between theoretical predictions for the ISM mass and observations. In an attempt to explain the deficiency in the ISM in the inner regions of NGC 205, we claim that efficient SN feedback capable of expelling gas/dust from the inner, star-forming regions of NGC 205 to the outer regions and/or tidal interactions with M31 stripping the gas/dust component from the galaxy provide the best explanation for the removal of a significant amount of the ISM from NGC 205. However, if SN feedback is found to lack responsibility for the removal of gas/dust from the inner regions, we might have to reconsider the importance of tidal interactions on the gaseous component in a galaxy within the tidal radius and/or revise the parameters characterizing the orbit of NGC 205 in its approach towards M31.

ACKNOWLEDGMENTS

REFERENCES

Baade W., 1951, Publ. Michigan Obser., 10, 7
Babul A., Rees M. J., 1992, MNRAS, 255, 346
Bekki K., Couch W. J., 2011, MNRAS, 415, 1783
Bekki K., Couch W. J., Drinkwater M. J., 2001, ApJ, 552, L105
Bendo G. J. et al., 2010, A&A, 518, L65
Bendo G. J. et al., 2012a, MNRAS, 419, 1833
Bendo G. J., Galliano F., Madden S. C., 2012b, MNRAS, in press (arXiv:1202.4629)
Bertola F., Bressan A., Burstein D., Buson L. M., Chiosi C., di Serego Alighieri S., 1995, ApJ, 438, 680
Bica E., Alloin D., Schmidt A. A., 1990, A&A, 228, 23
Block D. L. et al., 2006, Nat, 443, 832
Bolatto A. D., Leroy A. K., Rosolowsky E., Walter F., Blitz L., 2008, ApJ, 686, 948
Boquien M., Lisenfeld U., Duc P.-A., Braine J., Bournaud F., Brinks E., Charmandaris V., 2011a, A&A, 533, A19
Boquien M. et al., 2011b, AJ, 142, 111
Boselli A., Lequeux J., Gavazzi G., 2002, A&A, 384, 33
Boselli A., Boissier S., Cortese L., Gavazzi G., 2008, ApJ, 674, 742
Boselli A., Boissier S., Cortese L., Buat V., Hughes T. M., Gavazzi G., 2009, ApJ, 706, 1527
Bot C., Ysard N., Paradis D., Bernard J. P., Lagache G., Israel F. P., Wall W. F., 2010, A&A, 523, A20
Boylan-Kolchin M., Bullock J. S., Kaplinghat M., 2012, MNRAS, 422, 1203
Brosch N., Almoznino E., Heller A. B., 2004, MNRAS, 349, 357
Buckle J. V. et al., 2009, MNRAS, 399, 1026
Choi P. I., Guhathakurta P., Johnston K. V., 2002, AJ, 124, 310
Compiègne M. et al., 2011, A&A, 525, A103
Cormier D. et al., 2010, A&A, 518, L57
Currie M. J., Draper P. W., Berry D. S., Jenness T., Cavanagh B., Economou F., 2008, in Argyle R. W., Bunclark P. S., Lewis J. R., eds, ASP Conf. Ser. Vol. 394, Astronomical Data Analysis Software and Systems XVII. Astron. Soc. Pac., San Francisco, p. 650
Daddi E. et al., 2010, ApJ, 714, L118
Davidge T. J., 2003, ApJ, 597, 289
Davidge T. J., 2005, AJ, 130, 2087
Davies J. I. et al., 2010, MNRAS, 409, 102
De Rijcke S., Prugniel P., Simien F., Dejonghe H., 2006, MNRAS, 369, 1321
de Vaucouleurs G., de Vaucouleurs A., Corwin H. G., Jr, Buta R. J., Paturel G., Fouqué P., 1991, Third Reference Catalogue of Bright Galaxies. Volume I: Explanations and References. Volume II: Data for Galaxies between 0^h and 12^h. Volume III: Data for Galaxies between 12^h and 24^h. Springer, New York, NY
De Young D. S., Heckman T. M., 1994, ApJ, 431, 598
Dekel A., Silk J., 1986, ApJ, 303, 39
Demers S., Battinelli P., Letarte B., 2003, AJ, 125, 3037
Draine B. T., Li A., 2007, ApJ, 657, 810
Dumke M., Krause M., Wielebinski R., 2004, A&A, 414, 475
Eales S. A. et al., 2010, A&A, 518, L62
Eales S. et al., 2012, ApJ, submitted
Faber S. M., Gallagher J. S., 1976, ApJ, 204, 365
Fich M., Hodge P., 1991, ApJ, 374, L17
Fritz J. et al., 2012, A&A, submitted
Galametz M. et al., 2009, A&A, 508, 645
Galametz M. et al., 2010, A&A, 518, L55
Galametz M., Madden S. C., Galliano F., Hony S., Bendo G. J., Sauvage M., 2011, A&A, 532, A56
Gallagher J. S., III, Hunter D. A., Mould J., 1984, ApJ, 281, L63
Galliano F., Madden S. C., Jones A. P., Wilson C. D., Bernard J.-P., Le Peintre F., 2003, A&A, 407, 159
Galliano F., Madden S. C., Jones A. P., Wilson C. D., Bernard J.-P., 2005, A&A, 434, 867
Galliano F., Dwek E., Chanial P., 2008, ApJ, 672, 214
Galliano F. et al., 2011, A&A, 536, A88
Geha M., Guhathakurta P., Rich R. M., Cooper M. C., 2006, AJ, 131, 332
Gordon K. D. et al., 2006, ApJ, 638, L87
Gordon K. D. et al., 2007, PASP, 119, 1019

Gordon K. D., Engelbracht C. W., Rieke G. H., Misselt K. A., Smith J.-D. T., Kennicutt R. C., Jr, 2008, ApJ, 682, 336

Gordon K. D. et al., 2010, A&A, 518, L89

Griffin M. J. et al., 2010, A&A, 518, L3

Grossi M. et al., 2010, A&A, 518, L52

Guelin M., Zylka R., Mezger P. G., Haslam C. G. T., Kreysa E., Lemke R., Sievers A. W., 1993, A&A, 279, L37

Guelin M., Zylka R., Mezger P. G., Haslam C. G. T., Kreysa E., 1995, A&A, 298, L29

Haas M., 1998, A&A, 337, L1

Hildebrand R. H., 1983, Q. J. R. Astron. Soc., 24, 267

Ho L. C., Filippenko A. V., Sargent W. L., 1995, ApJS, 98, 477

Hodge P. W., 1973, ApJ, 182, 671

Hoeppe G., Brinks E., Klein U., Giovanardi C., Altschuler D. R., Price R. M., Deeg H.-J., 1994, AJ, 108, 446

Howley K. M., Geha M., Guhathakurta P., Montgomery R. M., Laughlin G., Johnston K. V., 2008, ApJ, 683, 722

Ibata R., Irwin M., Lewis G., Ferguson A. M. N., Tanvir N., 2001, Nat, 412, 49

Icke V., 1985, A&A, 144, 115

Israel F. P., Wall W. F., Raban D., Reach W. T., Bot C., Oonk J. B. R., Ysard N., Bernard J. P., 2010, A&A, 519, A67

James A., Dunne L., Eales S., Edmunds M. G., 2002, MNRAS, 335, 753

Johnson D. W., Gottesman S. T., 1983, ApJ, 275, 549

Karachentsev I. D., 2005, AJ, 129, 178

Kaufman M. J., Wolfire M. G., Hollenbach D. J., Luhman M. L., 1999, ApJ, 527, 795

Klein U., Giovanardi C., Altschuler D. R., Wunderlich E., 1992, A&A, 255, 49

Knapp G. R., Leighton R. B., Wannier P. G., Phillips T. G., Huggins P. J., 1980, ApJ, 240, 60

Koleva M., de Rijcke S., Prugniel P., Zeilinger W. W., Michielsen D., 2009, MNRAS, 396, 2133

Kormendy J., Fisher D. B., Cornell M. E., Bender R., 2009, ApJS, 182, 216

Larson R. B., Tinsley B. M., Caldwell C. N., 1980, ApJ, 237, 692

Lebouteiller V. et al., 2012, A&A, submitted

Leroy A., Bolatto A. D., Simon J. D., Blitz L., 2005, ApJ, 625, 763

Leroy A., Bolatto A., Stanimirovic S., Mizuno N., Israel F., Bot C., 2007, ApJ, 658, 1027

Lisenfeld U., Israel F. P., Stil J. M., Sievers A., 2002, A&A, 382, 860

Lisker T., Glatt K., Westera P., Grebel E. K., 2006, AJ, 132, 2432

Lucero D. M., Young L. M., 2007, AJ, 134, 2148

McConnachie A. W., Irwin M. J., Lewis G. F., Ibata R. A., Chapman S. C., Ferguson A. M. N., Tanvir N. R., 2004, MNRAS, 351, L94

McConnachie A. W., Irwin M. J., Ferguson A. M. N., Ibata R. A., Lewis G. F., Tanvir N., 2005, MNRAS, 356, 979

Madden S. C., 2000, New. Astron. Rev., 44, 249

Madden S. C., Geis N., Genzel R., Herrmann F., Jackson J., Poglitsch A., Stacey G. J., Townes C. H., 1993, ApJ, 407, 579

Madden S. C., Poglitsch A., Geis N., Stacey G. J., Townes C. H., 1997, ApJ, 483, 200

Madden S. C., Galliano F., Jones A. P., Sauvage M., 2006, A&A, 446, 877

Maraston C., 1998, MNRAS, 300, 872

Maraston C., 2005, MNRAS, 362, 799

Marleau F. R. et al., 2006, ApJ, 646, 929

Martín-Manjón M. L., Mollá M., Díaz A. I., Terlevich R., 2012, MNRAS, 420, 1294

Martins L. P., Lanfranchi G., Gonçalves D. R., Magrini L., Teodorescu A. M., Quireza C., 2012, MNRAS, 419, 3159

Mathis J. S., Mezger P. G., Panagia N., 1983, A&A, 128, 212

Mayer L., Governato F., Colpi M., Moore B., Quinn T., Wadsley J., Stadel J., Lake G., 2001, ApJ, 559, 754

Mayer L., Mastropietro C., Wadsley J., Stadel J., Moore B., 2006, MNRAS, 369, 1021

Meixner M. et al., 2010, A&A, 518, L71

Meny C., Gromov V., Boudet N., Bernard J.-P., Paradis D., Nayral C., 2007, A&A, 468, 171

Meurer G. R., 2010, in Treyer M., Wyder T. K., Neill J. D., Seibert M., Lee J. C., eds, ASP Conf. Ser. Vol. 440, UP2010: Have Observations Revealed a Variable Upper End of the Initial Mass Function? Astron. Soc. Pac., San Francisco, p. 189

Monaco L., Saviane I., Perina S., Bellazzini M., Buzzoni A., Federici L., Fusi Pecci F., Galleti S., 2009, A&A, 502, L9

Moore B., Katz N., Lake G., Dressler A., Oemler A., 1996, Nat, 379, 613

Müller T., Okumura K., Klaas U., 2011, PICC-ME-TN-038, available from the ESA Herschel Science Centre

Murphy E. J. et al., 2006, ApJ, 651, L111

Nulsen P. E. J., 1982, MNRAS, 198, 1007

O'Halloran B. et al., 2010, A&A, 518, L58

Ott S., 2010, in Mizumoto Y., Morita K. I., Ohishi M., eds, ASP Conf. Ser. Vol. 434, Astronomical Data Analysis Software and Systems XIX. Astron. Soc. Pac., San Francisco, p. 139

PACS Observer's Manual, 2011, HERSCHEL-HSC-DOC-0832, available from the ESA Herschel Science Centre

Parkin T. J. et al., 2012, MNRAS, 422, 2291

Pilbratt G. L. et al., 2010, A&A, 518, L1

Planck Collaboration et al., 2011, A&A, 536, A17

Poglitsch A. et al., 2010, A&A, 518, L2

Rice W., Lonsdale C. J., Soifer B. T., Neugebauer G., Kopan E. L., Lloyd L. A., de Jong T., Habing H. J., 1988, ApJS, 68, 91

Richer M. G., McCall M. L., 2008, ApJ, 684, 1190

Roussel H., 2012, ApJ, submitted

Sage L. J., Welch G. A., Mitchell G. F., 1998, ApJ, 507, 726

Sato N. R., Sawa T., 1986, PASJ, 38, 63

Savage B. D., Sembach K. R., 1996, ARA&A, 34, 279

Saviane I., Monaco L., Hallas T., 2010, in Bruzual G., Charlot S., eds, Proc. IAU Symp. 262, Stellar Populations – Planning for the Next Decade. Cambridge Univ. Press, Cambridge, p. 426

Sharina M. E., Afanasiev V. L., Puzia T. H., 2006, MNRAS, 372, 1259

Shetty R., Glover S. C., Dullemond C. P., Klessen R. S., 2011, MNRAS, 412, 1686

Smith M. W. L. et al., 2010, A&A, 518, L51

Smith M. W. L. et al., 2012, ApJ, 748, 123

Sollima A., Gil de Paz A., Martinez-Delgado D., Gabany R. J., Gallego-Laborda J. J., Hallas T., 2010, A&A, 516, A83

SPIRE Observer's Manual, 2011, HERSCHEL-HSC-DOC-0798, available from the ESA Herschel Science Centre

Stansberry J. A. et al., 2007, PASP, 119, 1038

Strong A. W. et al., 1988, A&A, 207, 1

Swinyard B. M. et al., 2010, A&A, 518, L4

Thilker D. A., Braun R., Walterbos R. A. M., Corbelli E., Lockman F. J., Murphy E., Maddalena R., 2004, ApJ, 601, L39

Tielens A. G. G. M., Hollenbach D., 1985, ApJ, 291, 722

Valluri M., Ferrarese L., Merritt D., Joseph C. L., 2005, ApJ, 628, 137

van den Bergh S., 1998, AJ, 116, 1688

Warren B. E. et al., 2010, ApJ, 714, 571

Weisz D. R. et al., 2012, ApJ, 744, 44

Welch G. A., Sage L. J., Mitchell G. F., 1998, ApJ, 499, 209

Wilcots E. M., Hodge P., Eskridge P. B., Bertola F., Buson L., 1990, ApJ, 364, 87

Wilson C. D., 1995, ApJ, 448, L97

Wilson C. D. et al., 2009, ApJ, 693, 1736

Young L. M., Lo K. Y., 1996, ApJ, 464, L59

Young L. M., Lo K. Y., 1997, ApJ, 476, 127

Zubko V., Dwek E., Arendt R. G., 2004, ApJS, 152, 211

This paper has been typeset from a TeX/LaTeX file prepared by the author.